Recent volcano-tectonic activity of the Ririba rift and the evolution of rifting in South Ethiopia

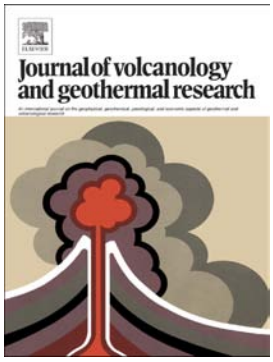

Recent volcano-tectonic activity of the Ririba rift and the evolution of rifting in South Ethiopia

Zara Franceschini, Raffaello Cioni, Stéphane Scaillet, Giacomo Corti, Federico Sani, Ilaria Isola, Francesco Mazzarini, Florian Duval, Asfaw Erbello, Ameha Muluneh, Sascha Brune

PII: S0377-0273(20)30182-7

DOI: https://doi.org/10.1016/j.jvolgeores.2020.106989

Reference: VOLGEO 106989

To appear in: *Journal of Volcanology and Geothermal Research*

Received date: 27 March 2020

Revised date: 26 June 2020

Accepted date: 27 June 2020

Please cite this article as: Z. Franceschini, R. Cioni, S. Scaillet, et al., Recent volcano-tectonic activity of the Ririba rift and the evolution of rifting in South Ethiopia, *Journal of Volcanology and Geothermal Research* (2020), https://doi.org/10.1016/j.jvolgeores.2020.106989

Recent volcano-tectonic activity of the Ririba rift and the evolution of rifting in South Ethiopia

Zara Franceschini[1,2], Raffaello Cioni[2,3], Stéphane Scaillet[4], Giacomo Corti[3,5], Federico Sani[2], Ilaria Isola[5], Francesco Mazzarini[5], Florian Duval[4], Asfaw Erbello[6], Ameha Muluneh[7], Sascha Brune[8]

[1]Dipartimento di Scienze della Terra, Università di Pisa, Pisa, Italy.

[2]Dipartimento di Scienze della Terra, Università degli Studi di Firenze, Florence, Italy.

[3]Istituto di Geoscienze e Georisorse, Consiglio Nazionale delle Ricerche, Florence, Italy.

[4]Institut des Sciences de la Terre d'Orléans (ISTO), UMR 7327 INSU-CNRS-BRGM – Université d'Orléans, France.

[5]Istituto Nazionale di Geofisica e Vulcanologia, Sezione di Pisa, Pisa, Italy.

[6]School of Applied Natural Sciences, Adama Science and Technology University, Adama, Ethiopia.

[7]School of Earth Sciences, Addis Ababa University, Addis Ababa, Ethiopia.

[8]German Research Centre for Geosciences GFZ, Potsdam, Germany.

Corresponding author: Zara Franceschini (zara.franceschini@phd.unipi.it)

Abstract

The relationships between volcanic activity and tectonics at the southernmost termination of the Main Ethiopian Rift (MER), East Africa, still represent a debated problem in the MER evolution. New constraints on the timing, evolution and characteristics of the poorly documented volcanic activity of the Dilo and Mega volcanic fields (VF), near the Kenya-Ethiopia border are here presented and discussed. The new data delineate the occurrence of two distinct groups of volcanic rocks: 1) Pliocene subalkaline basalts, observed only in the Dilo VF, forming a lava basement faulted during a significant rifting phase; 2) Quaternary alkaline basalts, occurring in the two volcanic fields as pyroclastic products and lava flows issued from monogenetic edifices and covering the rift-related faults. $^{40}Ar/^{39}Ar$ dating constrains the emplacement time of the large basal lava plateau to ~3.7 Ma, whereas the youngest volcanic activity characterizing the two areas dates back to 134 ka (Dilo VF) to as recent as the Holocene (Mega VF). Volcanic activity developed along tectonic lineaments independent from those of the rift. No direct relations are observed between the Pliocene, roughly N-S-trending major boundary faults of the Ririba rift and the NE-SW-oriented structural trend characteristic of the Quaternary volcanic activity. We speculate that this change in structural trend may be the expression of (1) inherited crustal structures affecting the distribution of the recent volcanic vents, and (2) a local stress field controlled by differences in crustal thickness, following a major episode of reorganization of extensional structures in the region due to rift propagation and abandonment.

Key words

Volcano-tectonic activity, continental rifting, rift evolution, inherited fabrics, $^{40}Ar/^{39}Ar$ dating, South Ethiopia

1 Introduction

Volcanic activity is an important aspect of continental rifting and displays significant variations in terms of styles, erupted volumes and magma characteristics in different rifts or rift sectors. This is typically interpreted as reflecting the influence of several parameters (e.g., mantle composition, lithosphere-asthenosphere boundary topography, asthenospheric temperature; e.g., White & McKenzie, 1989; White et al., 2008; Shillington et al., 2009) on magma production and migration. Additionally, variations in volcanic activity may reflect complex relations between tectonics and magma ascent to the surface (e.g., Corti et al., 2004; Wright et al., 2012; Keir et al., 2015; Muirhead et al., 2015), which are currently not fully understood.

The Main Ethiopian Rift (MER), in East Africa, is a classic example of interplay between tectonic and magmatic activity during rifting (e.g., Boccaletti et al., 1999; Ebinger & Casey, 2001; Casey et al., 2006; Abebe et al., 2007; Kurz et al., 2007; Beutel et al., 2010; Rooney, 2010; Rooney et al., 2011; Keir et al., 2015; Hutchison et al., 2016). It records all different stages of rift evolution and is characterised by significant volcanic activity spanning from the Oligocene to present (Hayward & Ebinger, 1996; Corti, 2009). However, despite recent improvements in the knowledge of single volcanic centres in Ethiopia (Hutchison et al., 2015, 2016; Martin-Jones et al., 2017; Siegburg et al., 2017; Lloyd et al., 2018; Fontijn et al., 2018; McNamara et al., 2018; Tadesse et al., 2018; Hunt et al., 2020), volcanic activity in many rift sectors still remains poorly documented.

The Ririba rift, at the southern termination of the MER (*Fig. 1a, b*), represents one significant example of these poorly known rift sectors. The rift is located in the region of interaction between the Ethiopian and the Kenyan rifts and is characterised by significant recent volcanic activity occurring in two volcanic fields (VFs) here referred to as Dilo and Mega VFs. In a recent study, Corti et al. (2019) suggested that the Ririba rift formed from the southward propagation of the Ethiopian rift during the Pliocene. By providing data on the Dilo VF and its relationship with rift-related tectonic activity, Corti et al. (2019) documented that the tectonic activity of the Ririba rift ceased close to the Pliocene-Pleistocene boundary, when faulting migrated in the central part of the Turkana depression within a narrow deformation belt directly linking the Ethiopian and Kenyan rifts.

In the present contribution, we extend the work of Corti et al. (2019) considering a wider area of study which includes both the Dilo and Mega VFs. In particular, we investigate thoroughly the volcanism of both fields by characterising the different types of volcanoes, their morphology and distributions in connection with regional structural features. We combine data on erupted magma volumes (and rates), new geochronological data with a morphological and statistical analysis of the eruptive vents in the two VFs in order to analyse the interplay in time and space between volcanism and rift tectonics. Our analysis reveals interactions between volcanism, regional tectonics, local geology and crustal topography that are characteristic of volcanic lineaments in rifted areas, which makes the area important for the study of such particular settings.

2 Tectonic setting

The MER is part of the East African Rift (EAR), a system of 80-100 km-wide rift valleys extending for several thousand kilometers in the eastern part of the African continent. This rift system comprises a succession of aligned tectonic basins, connecting the oceanic domains of the Red Sea and Gulf of Aden in the Afar depression with the Turkana basin in Kenya (Chorowitz, 2005). The EAR marks the incipient boundary between the Nubian and Somalian plates, that are moving away from each other at rates of 5-7 mm/year in a roughly E-W direction (Saria et al., 2014).

In the Turkana depression the MER and Kenyan rift overlap, giving rise to a complex region where extensional deformation is accommodated along a ~300 km-wide system of mainly extensional structures (Morley et al., 1992, 1999; Ebinger et al., 2000; Emishaw et al., 2019). The unusual breadth of the Turkana depression and its anomalous low topography are believed to be a consequence of the interplay between the terminations of the two main rift systems (MER, Kenyan rift) and the transversal (roughly NW-SE-trending) pre-existing Mesozoic basin of the Anza graben (Foster and Gleadow, 1996; Morley et al., 1992, 1999; Ebinger et al. 2000; Brune et al., 2017).

In South Ethiopia, deformation is mostly accommodated within the Ririba rift (*Fig. 2*), which is believed to represent the southern and poorly-developed tip of the MER, formed following the southward propagation of this rift into the Turkana depression (Ebinger et al. 2000; Bonini et al., 2005; Corti et al., 2019). Faulting in the area is accompanied by widespread, episodic volcanism (e.g., Brotzu et al., 1984; Hackman et al., 1990; Shinjo et al., 2011; Corti et al., 2019). In particular, three phases of volcanism have been described in the area (Brotzu et al., 1984; Shinjo et al., 2011): Middle Miocene (12.3-10.5 Ma), Late Miocene-Pliocene (6.1-3.6 Ma), Quaternary

(0.9-0.3 Ma). The Middle Miocene volcanism, which occurred north of the Ririba rift and did not develop in the area investigated in this study, was characterised prevalently by effusive activity producing alkaline basalts and hawaiites, which form a more or less continuous sheet covering a large area. Volcanism resumed during late Miocene-Pliocene (6.1-3.6 Ma), giving rise to a widespread tholeiitic lava platform, generally referred to as Bulal basalts, Gombe Group and Hurran Hurra lavas in Kenya, west of Lake Turkana (Hackman et al., 1990; Watkins, 1983). Quaternary volcanic activity was dominantly of central-type and characterised by the formation of hundreds of monogenetic centres (defined as volcanic edifices of small cumulative volume, generally ≤ 1 km^3, formed by one or several small eruptions in a relatively short time period and possibly showing a wide range of eruptive styles; Németh & Kereszturi, 2015) both sitting on the flanks of huge elliptical shield volcanoes, such as Huri Hills and Marsabit in Kenya, or aligned along minor structures in the whole area. Activity in the volcanic fields of Dilo and Mega developed during this phase and show a general NE-NNE-trending alignment of cinder cones and maars which erupted alkaline basaltic products (scorias, lava flows) often characterised by the presence of abundant mantle and basement (igneous and metamorphic rocks) xenoliths (Hackman et al., 1990; Orlando et al., 2006). Available K-Ar ages for the two areas range between 1.9 and 0.3 Ma (Brotzu et al., 1984; Shinjo et al., 2011), although the presence of black, unvegetated and unaltered lava flows in the Mega VF suggest very recent activity (Orlando et al., 2006). Both the Huri Hills and Dilo VFs overlie a Late Miocene-Pliocene lava platform, whereas, although there is no evidence of the Miocene-Pliocene fissural volcanic phase, in the Mega VF the Quaternary volcanic products lie either on earlier lava flows or directly on the Precambrian basement. In addition to the 5 samples already reported in Corti et al. (2019), new ^{40}Ar/^{39}Ar age data for this activity are presented here for the Mega VF, together with an extended morphological and statistical analysis of the eruptive vents in the two VFs. As we show below, these allow a better definition of the time limits for the last volcanic phases in the two VFs.

3 Analytical methods

Different, complementary approaches were integrated to characterise the volcanic activity in the two VFs, namely geological interpretation of remote sensing data, fieldwork, statistical analysis of vent clustering, and petrographic, compositional and ^{40}Ar/^{39}Ar geochronological analyses.

3.1. Fieldwork, remote sensing and morphometric analysis of volcanic edifices

The fieldwork was mainly focused on the collection of geological-structural data (analysis of the kinematics of the main faults and of their timing and relationships with volcanic activity), the characterisation of the different volcanic edifices and the volcanic stratigraphy, as well as sampling of volcanic rocks in both volcanic fields. In total, 36 samples (9 of which were already described in Corti et al., 2019; *Tab. S1 of Supplementary material*) of different volcanic rocks (e.g. lava flows, scoria and maar deposits) were collected for laboratory analyses.

Remote sensing analysis of the study area was conducted on the basis of satellite imagery (Google Earth and DigitalGlobe satellite images) and Digital Elevation Models (Shuttle Radar Topography Mission, SRTM, with 30 m resolution). Volcanic centres, eruptive fissures and some of the main lava flows (those presenting unequivocal morphological features) were

identified and characterised in order to differentiate the type of volcanism that took place in the two volcanic fields. The following morphometric parameters were measured (see *section S2 of Supplementary material* for details on methodology): basal and crater diameters (W_{co} and W_{cr}); cone height and crater depth (H_{co} and H_{cr}); area (A) of the cone; average slope (α). Besides these, H_{co}/W_{co}, W_{cr}/W_{co} and H_{cr}/W_{cr} ratios are also determined, where possible, to discriminate and quantify morphological differences between the different types of volcanic edifices in the two volcanic fields. Classification of the different cinder cones is based on the different types proposed by Bemis & Ferencz (2017). The volcanic edifices were also qualitatively distinguished in different classes of maturity mainly based on the criteria defined by Haag et al. (2019) derived from the critical analysis of the calculated morphometric data and recognition of textures and patterns on the high resolution (<5 m) Google Earth satellite images of the area (examples of different edifices attributed to the 4 different classes of maturity are shown in *Fig. S2c of Supplementary material*):

- young edifice: an edifice with well-defined crater and basal limits, lacking obvious gullies or erosional structures;
- moderately mature edifice: cones with a well-defined crater but displaying variable amount of gullies;
- mature edifice: a cone lacking a well-defined crater (i.e. rounded top) and showing evidence of ravines;
- old edifice: reduced, highly eroded landforms.

Where both W_{co} and W_{cr} are recognizable, an estimation of the volumes involved is obtained by assuming circular truncated cones with regular slopes (Jaimes-Viera et al., 2018). To calculate volumes of the main recognized lava flows, areal extents are multiplied by mean thicknesses averaged over several profiles along the flow run out. For lava flows characterised by irregular flow lobes, the area was subdivided in multiple sectors in order to reduce the error in the volume estimation. Remote analysis is also used to characterise the distribution of volcanic vents and their possible relations with tectonic structures.

3.2. Statistical analysis of vent clustering

The spatial distribution of volcanic vents in the Dilo VF conducted by Corti et al. (2019) was extended in this work studying vent clustering in both VFs through the analysis of the nearest neighbour distance distribution (or vent separation, *s*) and the application of the hierarchical cluster analysis of Mazzarini & Isola (2010). Vent density estimation and mapping of volcanic structures was then performed, along with the determination of the overall shape of the volcanic fields (direction of elongation of the ellipse approximating the volcanic field) by Principal Component Analysis (PCA) and the azimuthal distribution of segments connecting the different vents (i.e., the Vent-to-Vent Distribution, VVD) in the volcanic fields (Mazzarini et al., 2016; a detailed description of these methodologies is reported in *section S3 of Supplementary material*). Vent clustering and volcanic field shape analysis were then compared with the structures characterising the volcanic field, basement, and rift at regional scale in order to investigate the possible relationships between deep and shallow crustal structures and location and pattern of volcanism (e.g. Isola et al., 2014).

3.3. Petrographic and geochemical analyses

In the Dilo VF we collected 9 samples (also presented in Corti et al., 2019), whereas other 15 samples from lava flows and scoria cones were collected in the Mega VF (*Tab. S4 of Supplementary material*). Samples were powdered in an agata mortar and analysed for major (ICP-AES), trace elements (including rare earth elements; ICP-MS) and loss on ignition (LOI) at the ALS Laboratory Group of Sevilla (Spain). A petrographic study of the collected samples was then performed to confirm rock classification based on chemical composition and to take into account the possible influence of mafic enclaves and/or alteration on observed compositional variations.

3.4 Geochronology

$^{40}Ar/^{39}Ar$ step-heating dating was performed on the groundmass of 12 samples of lava flows (five of which presented in Corti et al., 2019) selected using stringent criteria for freshness. The samples were processed using standard means (crushing to a grain size ranging between 250-500 μm, followed by ultrasonic cleaning and hand-picking under a binocular microscope) to achieve the highest possible purity. After neutron irradiation in the CLICIT (Cd-lined) slot of Corvallis Nuclear Reactor (Oregon State University), $^{40}Ar/^{39}Ar$ measurements were performed at the CNRS-Orléans laboratory using a high-resolution Helix SFT mass-spectrometer outfitted to a CO_2-laser based extraction system featuring ultra-low argon blanks. Isotopic abundances were regressed back to inlet time and corrected for instrumental parameters (blank, mass discrimination, dead-time, post irradiation decay, atmospheric contamination) and neutron-induced isotopic interferences according to Scaillet (2000). The final data for each sample are reported as apparent age spectra against the cumulative ^{39}Ar released in order to illustrate their internal homogeneity (plateau age) or the lack thereof. These ages are complemented by the isotopic geochemistry of the released gas. $^{37}Ar_{Ca}$ and $^{36}Ar_{atm}$ are normalized to $^{39}Ar_K$ (^{39}Ar produced from ^{39}K during irradiation) and plotted in the form of isotopic ratios. ^{38}Ar was recorded as well, but does not provide any relevant information about chlorine due to irradiation under fast neutrons, which lowers the net yield of $^{38}Ar_{Cl}$ from thermal neutron capture on chlorine by a factor of 100 (Scaillet et al., 2011). Accordingly, the $^{38}Ar_{Cl}/^{39}Ar_K$ ratio is not reported in this paper.

4 Results

4.1. Volcanology

Within the several, small, generally monogenetic, volcanic landforms characterising the two VFs, it was possible to recognize volcanic cones, spatter ramparts, tuff rings and maars (*Fig. 3*). Several cinder cones were unequivocally recognized from analysis of satellite images basing on their association with lava flows; conversely, in many cases it was not possible to precisely define the nature of all other cones.

Cinder cones were recognized as steep-sided edifices formed by loose or partially welded pyroclastic fragments (Fornaciai et al., 2012; De Silva & Lindsay, 2015) and, as defined in literature, they are typically associated with lava flows directly fed by lava fountain activity or issued from the base of the cone. From remote and field observations it was possible to identify few lava flows associated with spatter ramparts, steep, linear features a few meters high formed during lava fountaining along a fissure. These lavas have in general a smaller areal extent than

those associated directly with a cone. Maars are nearly circular depressions with the crater floor lying below the pre-eruptive surface and are generally surrounded by low rims of ejected debris (tephra rings) or, occasionally, by tuff rings (White and Ross, 2011; De Silva & Lindsay, 2015; Lorenz et al., 2017). They are found in both the VFs, and they are often clustered. Tuff rings were differentiated by maars mainly basing on the depth of the crater floor with respect to the surrounding surface, and on the thicker pile of crater rim deposits. They occur sporadically in the two VFs and often difficult to characterise based on satellite images alone. These broad, low-profile edifices with the crater bottom lying below the surface can be distinguished from maar craters by the higher relief of their crater rim. Since maar craters are easier to detect and less affected by erosional processes, their concentration, inferred by remote sensing, is close to their true abundance. In contrast, all the volcanoes not amenable to quantitative morphometric analysis (red dots in *Figs. 4 and 5*) are more appropriately loosely classified as "old" cones.

4.1.1. Dilo Volcanic Field

The Dilo VF, located in the western part of the study area, includes the area surrounding the villages of Dilo and Gorai and extends across the Kenya-Ethiopia border (*Fig. 4*). The volcanic field is developed over a NE-SW-trending area covering about 1000 km^2 within the Ririba rift (*Fig. 2*) extending across the Kenya border, up to the Dukana village (about 50 km far from Dilo village).

The area is dominated by a faulted lava plateau that covers a wide region within and outside the rift, generated during a phase of intense fissural volcanic activity. The VF lays on top of this plateau. Satellite image analysis allowed to recognize a total of 52 volcanic vents (mainly represented by cinder cones) in the VF; among these, only 26 edifices (mainly maars, followed by cones) are still well preserved and could be used for morphometric data extraction (*Tab.1*). Lava flows, up to few meters thick and with a maximum length of 6.7 km, are often associated with cinder cones, in some cases covering the main faults of the Ririba rift (e.g., L29 and L30 in *Fig. 4*) (Corti et al., 2019). The area covered by the different lava flows ranges from 0.1 km^2 to the 16.9 km^2 of the largest flow (L29, *Fig. 4*), but usually is less than 2.5 km^2. Cones and maars are often found in clusters or aligned along specific trends, evidencing several main feeding fissures with a predominant NE-SW strike in the westernmost part of the field, while trending N-S/NNE-SSW near Dilo village (see below section 4.1.4). This change in direction can be clearly observed in the E-W-elongated shape of a maar north of the village of Gorai, or in the cluster of maars located south of Dilo (respectively M14 and M13 in *Fig. 4*). Cluster M13 is formed by three principal maars (two of them related to at least two volcanic explosions each) arranged along a NNE-SSW-trending alignment which also includes maar M11.

4.1.2. Mega Volcanic Field

The Mega VF, in the eastern part of the study area, includes the area around the villages of Mega and Megado. Its structures transversally cut the prominent Mega escarpment, an about 100 km-long, NW-SE trending structure with an average relief of 700 m (*Fig. 5*). In particular, the Mega VF develops on both sides of this escarpment covering an area of approximately 1400 km^2. Unlike the Dilo VF, where the recent volcanism always occurs on top of an old lava plateau, the floor of the Mega VF is more complex and characterised by Precambrian crystalline rocks (Orlando et al., 2006) and subordinated volcanic rocks of Pliocene age. The VF is formed

by several monogenetic centres of different nature and by large lava flows, which are always associated with cinder cones or, locally, with spatter ramparts (i.e. SR2, *Fig. 5*). Lava flow activity is clearly more relevant, in terms of number and volume, respect to the Dilo VF.

Compared to the Dilo VF, the Mega VF is characterised by a greater abundance of monogenetic centres (114), 41 of which have been used for morphometric analyses. Among these, cinder cones represent once again the dominant feature, while maars are less abundant (*Tab. 1*). With the exception of M7 (*Fig. 5*, a NE-SW-oriented cluster of three maars), maars mainly occur as individual volcanic centres. The most prominent maar feature of the area is El Sod (M1 in *Figs. 5 and 6*), which represents the widest and deepest maar of the Mega VF, with a diameter of 2.3 km and depth of 0.41 km. The presence of volcanic centres with different morphological maturity (*Tab. S2d of Supplementary material*) testifies for a prolonged duration of the monogenetic activity (or alternatively for the occurrence of multiple phases of activity). This is also testified by the occurrence of uneroded lava flows often partially overlying lava flows with a deeply eroded upper surface, whose feeder vents are no more clearly recognizable. The areal extent of the mappable lava flows varies from 0.1 km^2 to more than 28.8 km^2, with an average of 8.5 km^2. With a maximum runout of about 18.5 km, these flows are often significantly larger than those characterising the Dilo VF. Fissure-fed lava flows also occur in the Megado area as evidenced by NE-SW oriented spatter ramparts (e.g. SR2, *Fig. 5*), but are generally smaller than the lava flows related to cinder cones. These are often aligned on fractures feeding large lava flows (e.g. C8, *Figs. 5 and 6*; C30, *Fig. 5*). Among the largest and youngest lava flows characterising the Mega VF, the L12 flow dominates the area of Megado (*Figs. 4 and 6*), flowing for more than 10 km from the Mega escarpment in a SW direction and covering an area of about 25 km^2 over a gently dipping substrate. The very fresh, black, glassy appearance of the upper lava surface, along with the minimal vegetation coverage (mainly lichens) strongly suggest a very recent age. Field analysis indicates that the source of this lava flow is likely related to N-S-trending, few meters-wide dikes visible at the upper tip of the flow. In general, all the products of the VF are characterised by a great (though variable) abundance of large olivine- and pyroxene-bearing nodules (up to 20 cm in size).

4.1.3. Types of volcanic edifices, morphometric analysis, and volume/area estimates

The volcanic edifices identified in both VFs through remote sensing are shown in *Figs. 4 and 5 (for further information see Tabs. S2d-e of Supplementary material)*. In line with previous authors (e.g. Porter, 1972; Wood, 1980; Fornaciai et al., 2012; Kervyn et al., 2012), for morphological considerations we focused only on positive, cone-shaped volcanic features. The observed cones appear strongly stratified, generally characterised by outward dipping and reversely graded deposits with lapilli to block-bearing beds. The alteration of the deposits is often pervasive. Some of the cones can be defined as “parasitic cone”, “crater row cone” or “gully cone” (Bemis & Ferencz, 2017). Cones feeding lava flows often display typical “horseshoe" shapes (breached cones), suggesting that part of the crater and cone flanks were rafted away during lava flow effusion (Németh et al., 2011). Several morphometric parameters, including H_{co}, H_{co}/W_{co} and slope, commonly show a trend of progressive decrease over time due to the effects of erosion (Paez, 2006; Paez, 2010; Kereszturi & Németh, 2012 and references therein). W_{cr}/W_{co} ratios of the studied cones roughly fit the ideal ratio of 0.4, while H_{co}/W_{co} ratios are always lower than the ideal ratio of 0.18 defined by Porter (1972) and Wood (1980) for relatively young, regular-shaped and uneroded cinder cones (*Tab. S2d of Supplementary*

material). Indeed, the cones occurring in the two volcanic fields often show poorly-regular features (asymmetric base and/or lack of any evident crater).

Following Haag et al.'s (2019) criteria, the cones are categorized as very young, moderately mature, mature, and old (*Tab. S2d of Supplementary material*). Although the morphology of a volcanic edifice is a complex function of both external factors (e.g., erosion, climate settings, tectonics, etc.), rock type, volcanic landform and age (Kereszturi & Németh, 2012), descriptive and morphometric analyses evidence the presence of an important age range within the volcanic activity in the Mega VF. This is especially evident when comparing edifices of the same type; as an example, the two cinder cones C19 and C31 (*Figs. 3 and 5*) exhibit a typical "horseshoe shape" associated with the presence of a lava flow, which in the case of C31 appears to be poorly defined with scarcely recognizable lateral levees. This cinder cone is characterised by engraved flanks, a gentler slope (~13°) and minor aspect ratios (H_{cr}/W_{cr}= 0.094 and H_{co}/W_{co}= 0.062) with respect to C19, which exhibits less eroded (hence potentially younger) flanks with a more marked crater morphology (α ~20°, H_{cr}/W_{cr} = 0.2 and H_{co}/W_{co}= 0.11).

Maar craters are generally an order of magnitude wider than those of the other monogenetic volcanic edifices, having an average H_{cr}/W_{cr} = 0.1 (*Tab. S2e of Supplementary material*), in agreement with the mean value reported in the MaarVLS Database (Graettinger et al., 2018). Due to the high explosivity and depth of explosion, the associated deposits are characterised by the presence of a huge number of deep-seated xenoliths, variable in size (up to m-sized bombs), torn out from the walls of the diatreme (metamorphic basement) or directly transported from the source region (mantle-derived xenoliths), a typical feature observed also in other maars (e.g., Saucedo et al., 2017). The lava flow basement (with the characteristic columnar jointing) is often exposed in the inner walls of several maar craters (*Figs. 4 and 6*), just below the deposits related to the maar explosive phreatomagmatic activity, representing the intersection with the pre-eruption surface topography. The maar-forming deposits are generally represented by planar and cross-stratified layers of matrix-supported material, produced by dilute pyroclastic density currents, with thinner intercalations of clast-supported, coarse-grained deposits related to minor phases of pyroclastic fallout. Features of wet deposition are also sometimes present (accretionary lapilli bearing beds; soft sediment deformations of some beds). Ballistic blocks are abundant in both types of deposits. Lava flows are never found associated with these maars, according to the general features of maar volcanism. Especially in the Dilo VF, maars generally occur in clusters, arranged along regional lineaments and sometimes with overlapping explosion footprints, resulting in compound crater shapes with septa (ridges separating low points in a compound crater) and complex tephra rings (Graettinger et al., 2018). The observed depth and internal slopes of the maars are generally the result of a post-eruptive modification by erosional retreat of the wall and post-eruption infill of the crater.

Considered as a whole, the mean surface area of volcanic cones does not significantly change among the two volcanic fields (around 0.9 km^2; *Tab. S2d of Supplementary material)*. On the other hand, a significant variation can be observed for maar craters, which are remarkably larger in the Dilo VF (mean value of 3 km^2, against the 1.6 km^2 of Mega VF maars; *Tab. S2e of Supplementary material*). An estimate of the erupted volume produced by this monogenetic, Quaternary volcanism, is obtained by multiplying the mean volume averaged over the volcanic cones of each volcanic field with the respective total number of cones (comprehensive also of those excluded from the morphometric analysis), yielding values of about 10 km^3 and 3 km^3 of

surface deposits (which could be possibly halved if transformed into Dense Rock Equivalent, DRE, considering the very low amount of lithic fragments and assuming a deposit total porosity of about 50%; Pioli et al., 2008) for the Mega and Dilo VFs, respectively. Adding the volume of associated lava flows (roughly representing about 10% of the edifice volume and with a porosity not larger than 15%; Kereszturi et al. 2013), a total DRE volume of about 6 km^3 for the Mega VF (calculated over a total area of around 1400 km^2) and 1.8 km^3 for the Dilo VF (over an area of around 1000 km^2) can be estimated.

Conversely, it is very difficult to estimate the volume related to the lava products erupted during the subalkaline phase in the Dilo VF, due to the very discontinuous outcrops.

4.1.4. Spatial distribution of volcanic edifices

The spatial distribution of edifices in the two volcanic fields was investigated applying the methodology illustrated in Mazzarini & Isola (2010) and Mazzarini et al. (2016).

For each volcanic field, a first run of the steps of the hierarchical clustering analysis defined the highest possible number of significant clusters: 10 for the Dilo VF and 8 for the Mega VF. By evaluating the similarity at any step of the process, a second run was then performed for each data set, yielding values of 6 and 4 clusters for Dilo VF and Mega VF, respectively. Only clusters with more than three vents have been considered for further analysis (*section S3.3 of Supplementary material*).

Applying the PCA on the clusters identified within the volcanic field, we obtain a set of azimuth angles for the maximum axis which differ from the overall volcanic field elongation (*Fig. 7, central panels; section S3.3 of Supplementary material*). The Dilo VF shows the VVD peak that well fits the PCA azimuth (*Fig. 7a, left panel*), while in the Mega VF the VVD peak is rotated clockwise from the PCA azimuth by 10° (*Fig. 7b, left panel*).

The vent clustering and volcanic field shape parameters differ substantially from the basement and rift lineaments orientations at a regional scale suggesting a substantial independence of these different features. Specifically, inside the volcanic zone, the NE-SW trend (which dominates among the volcanic structures) is not represented by any of the observed tectonic fabrics (*Fig. 8*).

In addition, no clear relation can be observed between the Mega VF (and the volcanic structures within it) and the regional trend of tectonic lineaments (*Figs. 7b and 8*), while these cut across at high angle the NW-SE-trending Mega escarpment. On the other hand, the Dilo VF shows, in the westernmost part of the studied area, a 25° angle with respect to the NNE-SSW western border and a main, nearly N-S fabric near Dilo (*Fig. 8*).

4.2. Petrography and geochemistry

The basal lava flows of the faulted plateau of the Dilo VF are petrographically and geochemically different from the products of the monogenetic activity of the two VFs, which share instead similar compositional features. The basal lava flows are petrographically similar to the Pliocene tholeiitic basalts described by Shinjo et al. (2011) in this area (see also Corti et al., 2019). They are sub-aphyric with phenocrysts of plagioclase and minor olivine and pyroxene and

generally poorly vesicular and xenolith-poor (only sample MDZ04 shows the presence of pyroxene and olivine-bearing nodules, up to 10 cm in size).

Conversely, the products of the monogenetic activity of the two volcanic fields are generally porphyritic with olivine and clinopyroxene, while plagioclase is only present as a groundmass phase. Phenocrysts often display jagged faces, embayments and sieve-texture; crystal zoning and skeletal textures are also common. A prominent feature of all these products is the great abundance of pyroxene- and olivine-bearing, mainly mantle-derived nodules (Orlando et al., 2006) and quartz- and feldspars-bearing, basement-derived, xenoliths. The observed features correspond to those described by Shinjo et al. (2011) for the Quaternary alkaline lavas occurring in this area.

Juvenile material collected from maars was recognised basing on its textural and compositional homogeneity and relative abundance over the different stratigraphic beds forming the tephra ring. It is generally glass-bearing and more porphyritic, and the most common phenocrysts are olivine, pyroxene and plagioclase. Coarse, single xenocrysts of alkali feldspar, quartz and olivine deriving from xenoliths disaggregation are often present. Phenocrysts are usually present as anhedral, rounded or broken pieces, and are sometimes characterised by reaction rims (e.g., pyroxene, quartz); they also display jagged faces, sieve-texture and sometimes occur as skeletal phenocrysts, suggesting rapid, disequilibrium growth. Maar samples are extremely rich both in mantle nodules and metamorphic quartz- and feldspar-bearing xenoliths. Due to the abundance of xenocrysts and xenoliths, whole rock analysis was performed only on two maar samples, being similar (although more porphyritic) to the other products of monogenetic activity.

Major and trace element data of all the analysed samples are reported in *Tab. S4 of Supplementary material*. The two groups distinguished above on the basis of the petrographic features show clear compositional differences as well, in agreement with literature data: (i) a subalkaline group, with petrographical and geochemical features typical of tholeiitic basalts, belonging to the faulted plateau lava at the base of the Dilo VF (Corti et al., 2019); (ii) an alkaline group (nepheline-basanite, according to the classification of Le Maitre et al., 2002), representing the products of different monogenetic edifices from the two volcanic fields (*Fig. 9a*). The alkaline group shows a restricted range in SiO_2 (between 43-46 wt.%, with only one sample nearly reaching 48 wt.%; *Fig. 9a*; *Tab. S4 of Supplementary material*), which contrasts with the larger variability shown by FeO, MgO and CaO (although not clearly correlated with SiO_2 variation), and of trace element data. Alkaline products are characterised by values of TiO_2 < 2.75 wt.%, while subalkaline samples have TiO_2 values around 3.5 wt.%, in agreement with what reported by Shinjo et al. (2011) for the Pliocene and Quaternary groups, respectively. Alkaline and subalkaline groups are particularly well evidenced through the Zr/Nb ratio (*Fig. 9b*), constant and around values of 3.2 for the alkaline group and 8-9 for the subalkaline samples, in agreement with literature data for primary magmas of basanite-phonolite trend and continental tholeiites, respectively (Wilson, 2007).

4.3. Geochronology

Almost all the analysed samples yielded essentially flat $^{40}Ar/^{39}Ar$ age spectra, providing therefore confidence that the (preferred) plateau ages (PA) date the time of eruption and have not

been disturbed or reset by subsequent geological events. Results of this analysis are reported in *Tab. 2* and *Fig. 10*.

The two samples collected from the lava plateau of the Dilo VF (MDZ05 and MDZ12) yield two plateaux at 3.69 ± 0.01 Ma and 3.75 ± 0.03 Ma respectively (Corti et al., 2019). The rest of the samples (collected from both volcanic fields) belong to the most recent volcanic phase which is characterised by the formation of the widespread monogenetic centres prevalently sitting on the flanks of huge shield volcanoes and aligned along minor structures. $^{40}Ar/^{39}Ar$ dating of four samples collected in the Dilo VF (MDZ03, 06, 10, 13) yielded ages ranging between 0.3 and 0.13 Ma (Corti et al., 2019) for this volcanic phase that appears to have lasted until very recently in the Mega VF.

As it can be seen from *Tab. 2 and Fig. 10c*, two of the samples collected from Mega VF (MDZ17, 21) yield $^{40}Ar/^{39}Ar$ ages of 0.116 ± 0.005 Ma and 0.044 ± 0.008 Ma respectively, whereas the other four samples show slightly negative systematics (*Fig. 10a, e*). Two of these samples (MDZ20 and MDZ33) yield ages basically within error of zero, pointing to very young, Holocene, ages. For such youthful samples, the occurrence of apparent negative ages is not unexpected on account of the probability of obtaining a $^{40}Ar/^{36}Ar$ sample ratio very close to the atmospheric value (and sometimes below, resulting in a negative age). The final age obtained from pooling all the steps together falls within error of zero, permitting to assign a very young age to the emplacement of these flows.

The other two samples, MDZ27 and, to a much lesser extent, MDZ31, returned a negative age (-0.087 ± 0.012 Ma and -0.010 ± 0.004 Ma respectively) that falls outside the physically feasible range. Such negative systematics for MDZ27 may reflect contamination with some isobar of ^{36}Ar (i.e., hydrochloridric $^{1}H^{35}Cl$) that the mass-spectrometer cannot resolve, leading to an overcorrection of the atmospheric ^{40}Ar (hence a negative age for a very young sample). In the case of MDZ27 it is also associated with an unusual increasing $^{36}Ar_{atm}/^{39}Ar_{K}$ trend during progressive degassing. This pattern is correlated with higher $^{37}Ar/^{39}Ar$ ratios (*Fig. 10e*) indicating a calcic phase like plagioclase as the probable carrier of this atmospheric-rich component.

While not optimal, the data from MDZ27 and MDZ31 concur with the data from the companion flows indicating a very young age consistent with the very young morphological aspect of the black lava flows south of Megado that can be categorized as the youngest products of the area.

5 Discussion

5.1. Phases and age of volcanism

Tectonic activity in Southern Ethiopia has been accompanied by voluminous and widespread magmatism, as observed in other MER sectors. This activity was episodic rather than continuous in time (e.g., Corti, 2009; Hutchison et al., 2016). Petrographic and geochemical analyses indicate the occurrence of two different groups of rocks (subalkaline and alkaline basalts) that can be referred to as the two most recent volcanic phases. Lavas from the first group (subalkaline

basalts) are only present in the Dilo VF and can be related to the same voluminous volcanic phase which generated the Pliocene tholeiitic Bulal basalts described in Kenya by Brotzu et al. (1984) and Shinjo et al. (2011), subsequently faulted during the later episodes of southward MER propagation in the Ririba rift (Corti et al., 2019). $^{40}Ar/^{39}Ar$ dating confirms this interpretation: the samples yield a Plateau Age (PA) of 3.69 ± 0.01 Ma for MDZ05 and of 3.75 ± 0.03 Ma for MDZ12 (Corti et al., 2019), corresponding to the K-Ar age range reported for the Bulal basalts in Brotzu et al. (1984) and Shinjo et al. (2011).

Unlike the subalkaline rocks, alkaline basalts were erupted in both areas, showing great affinities between the Dilo and Mega VFs. Their petrographic features, along with their prevalently basanite-dominated signature are closely similar to the products of the Quaternary volcanic phase described in the area by several authors (e.g., Brotzu et al., 1984; Shinjo et al., 2011). $^{40}Ar/^{39}Ar$ ages confirm this, indicating Late Pleistocene ages, with all samples being younger than 0.164 Ma. In particular, the new dataset presented in Corti et al. (2019) for the Dilo VF suggests that monogenetic volcanic activity in this area lasted until at least 0.134 ± 0.004 Ma (MDZ10), significantly younger than previous K-Ar data (0.29 ± 0.12 Ma) had suggested (Shinjo et al., 2011). Our new $^{40}Ar/^{39}Ar$ data are of particular relevance as they also comprise the first ages for the Mega VF. Here, the last volcanic activity was probably even much younger, as four samples from this area yield near-zero ages (Holocene ages), in agreement with the morphometric analysis of the cinder cones of the Mega VF, as well as with the very fresh, youthful, appearance of some lava flows (e.g., the large L12 lava flow south of Megado; *Fig. 5*).

5.2. Rates of volcanism

In both areas, the Quaternary monogenetic volcanism is characterised by cinder cones, maars, tuff rings and lava flows, with the Mega VF showing a slightly higher density of volcanic centres and associated lava flows than the Dilo VF (approximately $8 \times 10^{-2}/km^2$ vs. $5 \times 10^{-2}/km^2$, respectively). The new $^{40}Ar/^{39}Ar$ datings presented here define a minimum temporal interval of 160 kyr for the alkaline, monogenetic activity of the Dilo VF and of 110 kyr for Mega VF. The magma output rate (obtained dividing the total estimated volume DRE by the duration of volcanism), for the two VFs confirms the more intense activity of Mega VF (5.5×10^{-5} km^3/yr) respect to Dilo VF (1.1×10^{-5} km^3/yr). This difference also remains if magma output rates are normalized to the VF area (4.0×10^{-8} $km^3/km^2/yr$ and 1.1×10^{-8} $km^3/km^2/yr$, for Mega and Dilo VFs, respectively). When compared with the database of White et al. (2006), the calculated values of output rates fall between the lowest recorded at a global scale, typical of the low tail of the distribution of the output rate values for continental volcanic fields. Conversely, number per area density of volcanic centres in the two VFs does not differ from the average value at a global scale (Le Corvec et al., 2013) and it is one order of magnitude lower respect to that calculated from the data of Hunt et al. (2020) on a northernmost axial sector of the MER in the areas of Butajira and Ziwai ($3.3 \times 10^{-1}/km^2$ and $5.6 \times 10^{-1}/km^2$, respectively). This possibly reflects to the most relevant focussing role on magma ascent and emplacement played by rift-related faults respect to the off-axis fissures which characterize the Dilo and Mega VF.

An important feature of the Quaternary alkaline magmatism observed in the two VFs is the presence, in different amounts, of pyroxene and olivine-bearing, dm-sized nodules. Although detailed analyses were not performed on these nodules, their mineralogical and isotopic composition has been the subject of detailed previous works (e.g. Conticelli et al., 1999; Orlando

et al., 2006; Casagli et al., 2017; Alemayehu et al., 2016, 2017) and suggests an upper mantle provenance for this material. The abundance of these dense, mantle-derived xenoliths is suggestive of high magma ascent rates (> 0.5 ms^{-1} for a xenolith of 15 cm radius in a mafic magma; Spera, 1980), implying the lack of important intermediate reservoirs or stalling zones in which nodules would have sunk during the alkaline, more recent phase of activity in the two VFs. If interpreted in terms of associated plutonic activity, this suggests that the Quaternary alkaline volcanism was possibly less prone to form large crustal intrusions of magma with respect to the preceding Pliocene phase, thereby enlarging the gap in the magma production rate between these two phases of activity.

Finally, the analysis of the different volcanic vents in the two study areas reveals that the Quaternary volcanic features often show slightly elongated shapes and are found in clusters or as part of trending alignments. These observations indicate a strong relation between volcanic activity and tectonic structures, which is discussed in the following sections.

5.3. Styles of volcanic activity

The basaltic magma composition and the prevalence of cinder cones and associated lava flows over maars and tuff rings clearly indicate that Quaternary monogenetic volcanic activity in the Mega and Dilo VFs was mainly of Strombolian and Hawaiian type. Lava flow activity was present in both the areas, although being more developed (in terms of frequency and erupted volumes; *Tab. S2d of Supplementary material*) in the Mega VF. Volcanic activity was fed by nearly primary magma rapidly ascending from the source region (in order to transport large, crystal-bearing, mantle-derived xenoliths) and with high effusion rates able to sustain the emplacement of more than 10 km-long lava flows (from some tens to 100 m^3s^{-1}; Pinkerton & Wilson, 1994). Phreatomagmatic activity was also present in the two VF, possibly being more important in the Dilo VF, where maars and tuff rings represent at least 30% of the total of the observed edifices, respect to the Mega VF (where such edifices represent less than 10% of the total; *Tab. 1*).

While magmatic activity in the Mega VF was more pronounced in terms of erupted volumes, areal density of vents, and magma output rate, morphological parameters like W_{cr}/W_{co} or H_{co}/W_{co} of the monogenetic centres of the Dilo VF are generally lower than those measured for the Mega VF (*Tab. S2d of Supplementary material*), possibly reflecting a higher explosivity for the activity of the Dilo VF. Similarly, the phreatomagmatic centres of the Dilo VF, although with crater diameters of similar size, are characterized by a broader dispersal of the associated products with respect to those of the Mega VF (A_{co} of 3.0 and 1.6 km^2 for the Dilo and Mega VFs, respectively; *Tab. S2e of Supplementary material*), suggesting also in this case a higher explosivity. The evident clustering of maars in the Dilo VF and their alignment along structural lineaments also suggest an important control of deep-seated structures on this activity, in agreement with the average Elongation value (EL, *Tab. S2e of Supplementary material*) lower than the value calculated by Graettinger (2018) for the global maar database (0.70-0.75 vs. 0.81, respectively). We can so conclude that the most prominent role of phreatomagmatic activity, the generally higher explosivity of the activity, and the less abundant effusive activity in the Dilo VF respect to the Mega VF are possible indications of differences in the primary magmatic explosivity of erupted magma and of a different subsurface structural setting for the two VFs, which control the final magma ascent to the surface.

When compared with monogenetic volcanic fields at a global scale, the value of the H_{co}/W_{co} of the monogenetic cones for the two VFs is lower than the average value measured at other volcanic fields (Fornaciai et al., 2012), suggesting that intensity of the cone-building eruptions in this area was on average higher than the intensity of similar eruptions in other volcanic contexts.

5.4. Rifting, volcanism and the influence of pre-rift structures

In line with previous findings (Corti et al., 2019), data from remote analysis, fieldwork and $^{40}Ar/^{39}Ar$ geochronology delineate complex relationships between rift structures and volcanic evolution.

Specifically, the basal lava flows of the Dilo VF are affected by the main boundary faults of the Ririba rift, indicating that volcanic activity at ~3.7 Ma preceded or possibly coincided with the development of the Ririba rift, which in turn resulted from the southward propagation of the Main Ethiopian Rift in the area (Corti et al., 2019). This important phase of fissural activity, resulting in the widespread plateau of the Bulal lavas, may be related to a phase of more diffuse deformation during the Late-Miocene-Early Pliocene, as supported by numerical modelling (Corti et al., 2019).

The subsequent phase of Quaternary alkaline volcanic activity in the Dilo VF is by far less voluminous and post-dates the Ririba rift as testified by the present $^{40}Ar/^{39}Ar$ data. The main boundary faults of the rift are indeed sealed by two large lava flows dated at 153 ± 6 ka and 164 ± 7 ka, documenting the recent inactivity of rift-related structures in this area. Rift deactivation likely occurred close to the Pliocene-Pleistocene boundary, as indicated by rift-related faults covered by the basal flows of the Huri Hills edifice (Corti et al., 2019), immediately south of the study area. Analysis of the current distribution of deformation, together with numerical modelling of rift evolution, indicate that rifting in the area probably ceased because of focusing of the tectono-magmatic activity to the north and west of the area, in connection with the direct linkage of the Kenyan rift with the Ethiopian rift (Corti et al., 2019).

Statistical analysis of spatial distribution of the volcanic centres (*Figs. 7* and *8*), as well as their morphological features (*Fig. 3*), clearly demonstrate that activity occurred along NE-SW and NNE-SSW trends in the two volcanic fields (*Fig. 7*), similar to other volcanic centres in the region (e.g., Huri Hills and Marsabit volcanoes, Kenya; *Fig. 11*).

This suggests no direct relationship between the structure driving volcanic activity and the roughly N-S major boundary faults of the Ririba rift. Similarly, no direct relations are observed between volcanic alignments and the outcropping basement fabrics in the study area (*Fig. 8*). However, at a larger regional scale, the presence of pre-existing structures paralleling the overall elongation of Quaternary volcanic fields (i.e., with a NE-SW/NNE-SSW trend) suggest that the distribution of volcanic centres may have been controlled by these major inherited structures, such as the Buluk fault zone, west of the Ririba area (*Fig. 11;* e.g., Vetel & Le Gall, 2006; Corti et al., 2019). These structures have a very weak geomorphologic expression and are evident only due to the alignment of the volcanic centres. However, the associated structures necessarily extend at depth, potentially allowing the rapid ascent of mafic magma, and cut across major NW-SE oriented, pre-existing, large topographic structures such as the Mega escarpment. At a more local scale, the distribution of vents and their preferential elongation directions (within the single

volcanic fields) suggests a second-order control by inherited basement structures, as documented by angular networks of minor normal faults observed in the area (*Fig. 8*).

5.5. Buoyancy-driven effects on regional field stress and magma ascent

Since alignments of the vents are unrelated (i.e. oblique) to rift-related faults, a central question remains the significance of the major feeding structures of the volcanic fields. This anomalous orientation cannot be explained by a variation in the extension direction from roughly E-W to NW-SE during the Quaternary (e.g., Strecker & Bosworth, 1997), as recent plate kinematic models (e.g., Iaffaldano et al., 2014; DeMets & Merkouriev, 2016) do not support changes in the relative motion between Nubia and Somalia during the Pliocene-Quaternary. Similarly, structural and kinematic modelling of the architecture of Ethiopian rift (Corti, 2008; Erbello & Kidane, 2018), as well as the absence of NE-SW-trending normal faults in the Ririba rift and surrounding areas, argue against variations in far-field stresses.

Our analysis of the volcanic fields shows that their elongation is sub-parallel to the topographic and crustal thickness gradients connecting the eastern plateaus (elevation > 2000 m asl, crustal thickness > 40 km) with the Turkana depression (elevation < 1000 m asl, crustal thickness < 30 km; *Fig. 11*; e.g., Woldetinsae & Götze, 2005; Benoit et al., 2006; Sippel et al., 2017). These gradients generate buoyancy-related forces (Artyushkov, 1973; Brune, 2014), and induce tension in elevated areas and compression in lowlands. The resulting stress components are superimposed to the regional stress field and may result in a rotation of the principal axes if the magnitude of the buoyancy-related forcing is comparable to that of the background stress. We estimate the horizontal force resulting from crustal buoyancy variations using the formulation of Buck (1991)

$F_{cb} = g\,\Delta\rho\,h\,\delta h$, where $\Delta\rho = \rho_c(\rho_m - \rho_c)/\rho_m$,

with ρ_c and ρ_m being crust and mantle densities, g is the gravitational acceleration, h the reference crustal thickness of the Ethiopian plateau and δh the difference between crustal thickness of the plateau and the Turkana depression. For a crustal thickness of 40-43 km for the Ethiopian plateau and 27-30 km for the thinned Turkana area, we estimate a buoyancy force F_{cb} ranging between 1.3 and 2.3 TN/m (*Fig. 11*). This is a first-order estimate under the assumption of local isostatic equilibrium and small crustal thickness variations (Fleitout & Froidevaux, 1982; Buck, 1991). However, it is comparable to plate driving forces such a ridge push of about 3 TN/m (Bott, 1991; Turcotte & Schubert, 2002). Hence, we speculate that once the rifting ceased and the plate-related extensional stress field faded in the area, these buoyancy forces became dominant and may have resulted in the development of a stress field with maximum horizontal stress orthogonal to the roughly NW-SE Turkana depression, facilitating magma emplacement along NE-SW pre-existing structures.

5.6. Differences with other rift sectors and general implications

The lack of direct relations between major rift-related faults and the alignments of Pleistocene volcanic vents in the Dilo and Mega VFs contrasts with the central and northern sectors of the MER, where the recent volcanic centers are directly related to the Wonji faults affecting the axial portions of the rift and facilitating magma ascent (Corti, 2009). This significant difference is

possibly related to the contrasting thermal and rheological conditions of the Ririba rift with respect to other MER sectors. In regions where rifting is more advanced (e.g., Northern MER) the continental lithosphere has been deeply altered by rift-related thermal and mechanical processes: in these conditions, the axial tectono-magmatic systems may directly respond to far-field stresses and form perpendicular to the regional extension direction imposed by plate motion (e.g., Corti, 2009). In contrast, the rifting process in South Ethiopia occurs in a region where the crust/lithosphere system is still not significantly thermally and mechanically modified by rifting, and the local stress field has been significantly modified by abandonment of Ririba rift occurred at least by the end of Pliocene (Corti et al., 2019, and discussion above). In these conditions, volcanic alignments did not form perpendicular to the far-field extension direction as in other MER sectors (e.g., Northern MER), and are controlled by pre-existing structures oblique to rift-related structures. Therefore, the complex interactions among the local stress field and the presence of inherited fabrics may result in elongation of volcanic fields which may not necessarily represent the contemporaneous large-scale stress field imposed by plate motion.

Overall, the Ririba example supports that pre-existing structures may represent zones of crustal weakness that magma can exploit during its ascent (e.g., Le Corvec et al., 2013; Wadge et al., 2016), controlling the volcanic spatial and temporal evolution, volcanic morphology, magma volume, and eruptive dynamics (e.g., Gómez-Vasconcelos et al., 2020). This is similar to what observed in other regions undergoing extension (e.g., other portions of the East African Rift, Isola et al., 2014; the Tyrrhenian sea extensional system, Acocella & Funiciello, 2006; the Magellan Neogene Rift System, Mazzarini & D'Orazio, 2003; the Trans-Mexican Volcanic Belt, Gómez-Vasconcelos et al., 2020). Importantly, this suggests that the presence and reactivation of inherited fabrics may strongly control the characteristics of volcanic fields (i.e. volcanic field shape, vent alignment, feeder-dike pattern) and locally complicate the use of magmatic features as indicators of the regional present or past stress-field orientation.

6 Conclusions

In this study, we analysed the timing, evolution and characteristics of the volcanic activity of the volcanic fields of Mega and Dilo, at the southern termination of the Main Ethiopian Rift.

Our study supports the occurrence of two groups of rocks related to two different volcanic phases in the area: a group of rift-related, Pliocene subalkaline basalts, observed only in the Dilo VF, and a group of Quaternary alkaline basalts. New $^{40}Ar/^{39}Ar$ dating indicates ages of ~3.7 Ma for the subalkaline basalts, erupted and then faulted during an important rifting phase. $^{40}Ar/^{39}Ar$ dating of the alkaline basalts indicates that this activity, whose products cover the rift-related faults, dates back to 134 ka for Dilo and up to the Holocene for the Mega VF.

The Quaternary monogenetic volcanic activity generating the two volcanic fields is characterised by the eruption of mafic magma, punctuating the two areas with cinder cones, maars, tuff rings and associated lava flows. In terms of output rate and density of volcanic centres, the Mega VF was more active with respect to the Dilo VF, while type and morphology of the monogenetic centres possibly suggest a higher explosivity of the volcanic activity in the Dilo VF.

The general presence of large, mantle-derived xenoliths in all the alkaline basalts testifies for high magma ascent rates and implies a minor role of shallow magma reservoirs or stalling zones. Accordingly, plutonic activity was possibly reduced during this magmatic phase with respect to the rift-related, Pliocene phase accompanying the formation of Ririba rift. Further analyses are however required to gain a deeper understanding of the processes of magma genesis related to this activity.

No direct relationships are observed between the Pliocene, roughly N-S-trending major boundary faults of the Ririba rift and the Quaternary volcanic activity, which is generally distributed along NE-SW-trending lineaments. Such distribution is inferred to have been controlled by pre-existing fabrics, stress re-orientation due to gradients in crustal thickness, and/or reorganization of extensional structures related to rift propagation and abandonment, rather than by far-field stresses.

Acknowledgments

This research was supported by the National Geographic Society (Grant #9976-16) and by the Ministero Università e Ricerca (MiUR) through PRIN grant 2017P9AT72. We thank the DigitalGlobe Foundation for providing the satellite images in *Fig. S2b of Supplementary material*. The $^{40}Ar/^{39}Ar$ facility at ISTO was funded and is supported by the ERC Advanced grant RHEOLITH (grant agreement No 290864), the LABEX project VOLTAIRE (ANR-10-LABX-100-01), the Région Centre project ARGON, and the project EQUIPEX PLANEX (ANR-11-EQPX-0036).

Data availability

Datasets related to this study can be found at DOI:10.17632/4cb2cngpf2.1, online data repository hosted at Mendeley Data.

Figure 1. a) Quaternary faults, seismicity and Quaternary volcanoes in the Turkana depression and surrounding regions superimposed on a SRTM (Nasa Shuttle Radar Topography Mission, with 30 m resolution) digital elevation model (modified from Brune et al., 2017). Seismicity from USGS National Earthquake Information Center (NEIC) catalogue (1900 - present); volcanoes from the Smithsonian Institution, Global Volcanism Program database. CB: Chew Bahir basin; SB: Segen basin; LR: Lokichar basin; D: Dukana volcanic field; HH: Huri Hills; KS: Kino Sogo belt; LAB: Lake Abiyata; LL: Lake Langano; LS: Lake Shala; LA: Lake Abaya; LC: Lake Cha'mo; LCB: Lake Ch'ew Bahir; LT: Lake Turkana; M: Mega volcanic field; MV: Marsabit volcano; RR: Ririba rift. Black square indicates the investigated area, illustrated in *Fig. 2*. **b**) Schematic fault pattern and present-day plate kinematics of the East African Rift. Black arrows show relative motions with respect to a stable Nubian reference frame according to the best-fit model of Saria et al. (2014). Values besides arrows indicate motion in mm/yr. NU: Nubian plate; SO: Somalian plate; VI: Victoria microplate. Yellow square indicates the area portrayed in panel "**a**".

Figure 2. Geology of the Ririba rift superimposed on a SRTM (Nasa Shuttle Radar Topography Mission) digital elevation model (modified from Corti et al., 2019; Shinjo et al., 2011). Available ages in the area are taken from literature (references within the legend). White boxes indicate the area illustrated in *Fig. 4* (Dilo VF) and *Fig. 5* (Mega VF).

Figure 3. a) Types of volcanic centres observed in the two volcanic fields: C31 (older cone, Mega VF), C19 (younger cone, Mega VF), M1 (maar of El Sod, Mega VF), TR1 (tuff ring, Dilo VF). The red lines show one of the four profiles used for the determination of the morphological parameters; **b**) morphological profiles along the red lines shown in the four edifices in a) (data: Google, CNES/Airbus; Google, Maxar Technologies).

Figure 4. Google Earth satellite image (top) and SRTM digital elevation model (bottom) of the Dilo volcanic field, with superimposed volcanic edifices and principal lava flows (data: Google, Maxar Technologies, CNES/Airbus).

Figure 5. Google Earth satellite image (left) and SRTM digital elevation model (right) of the Mega volcanic field, with superimposed volcanic edifices and principal lava flows (data: Google, Landsat/Copernicus; Google, US Dept of State Geographer).

Figure 6. a) Lava flow (L12) to the South of Mega escarpment (Mega VF); **b**) elongated scoria cones along a NE-trending fissure (Mega VF); **c**) series of scoria cones (Mega VF); **d**) maar El Sod (Mega VF); **e**) Lava flows (with the characteristic columnar jointing) exposed in the inner crater walls of Maar Gorai (M18; Dilo VF); f) Up to m-sized bombs and blocks situated upon the ridge between two maars (M13; Dilo VF) and torn from the walls of the diatreme because of the high explosivity of the activity.

Figure 7. Rose diagrams of PCA azimuth and VVD analysis. *Left panel*: VVD plot and azimuth of the maximum axis of the ellipse (approximating the volcanic field) from PCA analysis (red solid line). *Central panel*: rose diagram of the azimuth of the maximum axis of ellipse from PCA analysis applied to clusters in the volcanic fields. *Right panel*: rose diagram of the azimuth of the volcanic structures in volcanic fields (see *Fig. S2b of Supplementary material*). **(a)** Dilo volcanic fields, azimuths from PCA analysis from *section S3.3 of Supplementary material*. **(b)** Mega volcanic fields, azimuths from PCA analysis from *section S3.3 of Supplementary material*.

Figure 8. Distribution of structural and volcanic features in the Dilo and Mega areas.

Figure 9. **a**) Total Alkalies vs. SiO_2 diagram for selected rocks from the literature and data from this work. The green line separates the fields of alkaline and subalkaline rocks. Pliocene rocks (in red) all plot in the subalkaline field, while Quaternary rocks (in blue) have an alkaline affinity; **b**) Zr vs. Nb diagram showing the different trends related to the alkaline Quaternary and subalkaline Pliocene products from the studied area and the surrounding regions.

Figure 10. $^{40}Ar/^{39}Ar$ analysis of samples collected from Mega VF (panels **a**, **c**, **e**) and from Dilo VF (panels **b**, **d**, **f**). Each panel illustrates the $^{40}Ar/^{39}Ar$ data of two samples, reporting the $^{37}Ar_{Ca}/^{39}Ar_K$ and $^{36}Ar_{atm}/^{39}Ar_K$ ratios for the released gas (upper graph) and Plateau Age (PA) with the respective estimated error (lower graph). N refers to the number of steps included in the calculation relative to the total extracted. WMA represents the Weighted Mean Age obtained excluding the indicated steps from the computation. MSWD is the Mean Square of Weight Deviates and provides a measure of data scatter relative to analytical precision. Arrows span consecutive steps included in the PA and WMA. Boxes represent the heating-steps, with the width of the box representing the percentage of ^{39}Ar released and its thickness corresponding to the analytical error (lower and upper limits of the uncertainty at $\pm 1\ \sigma$).

Figure 11. a) SRTM digital elevation model showing a possible link between the main orientation of the Quaternary volcanic fields of Dilo, Mega and Huri Hills (orange ellipses) and major inherited structures (dashed lines in the figure) such as KFZ (Kataboi Fault Zone) and BFZ (Buluk Fault Zone) (Vetel & LeGall, 2006). **b**) Moho depth of the study region (Sippel et al., 2017); black lines represent the trend of the volcanic fields main axis (D: Dilo VF; M: Mega VF; HH: Huri Hills; MV: Marsabit volcano). **c**) Estimated range of buoyancy-related forces due to crustal thickness gradients in the study region (see text for details).

Table 1. Number of cones (C), maars (M) and tuff rings (TR), considering the number of identified vents in each volcanic field (VF). *Note that the real number of cones is actually much higher considering that all the vents which were not considered form morphometric analysis are most likely cones.

Table 2. Summary table reporting the twelve analysed samples. MDZ03 to MDZ13 belong to Dilo VF; MDZ17 to MDZ33 belong to Mega VF.

References

Abebe, W.B., Douven, W.J.A.M., McCartney, M., & Leentvaar, J. (2007). EIA implementation and follow up: a case study of Koga irrigation and watershed management project Ethiopia (Doctoral dissertation, Unesco-IHE).

Acocella, V., & Funiciello, R. (2006). Transverse systems along the extensional Tyrrhenian margin of central Italy and their influence on volcanism. Tectonics, 25(2). https://doi.org/10.1029/2005TC001845

Alemayehu, M., Zhang, H.F., & Aulbach, S. (2016). Evaluation of mantle processes in an extensional regime: Insight from in situ O and Sr isotope systematics of mantle xenoliths from Ethiopia. The Journal of Geology, 124(5), 603-616. https://doi.org/10.1086/687754

Alemayehu, M., Zhang, H.F., & Sakyi, P.A. (2017). Nature and evolution of lithospheric mantle beneath the southern Ethiopian rift zone: evidence from petrology and geochemistry of mantle xenoliths. International Journal of Earth Sciences, 106(3), 939-958. https://doi.org/10.1007/s00531-016-1342-z

Artyushkov, E.V. (1973). Stresses in the lithosphere caused by crustal thickness inhomogeneities. Journal of Geophysical Research, 78(32), 7675-7708. https://doi.org/10.1029/JB078i032p07675

Bemis, K.G., & Ferencz, M. (2017). Morphometric analysis of scoria cones: the potential for inferring process from shape. Geological Society, London, Special Publications, 446(1), 61-100. https://doi.org/10.1144/SP446.9

Benoit, M.H., Nyblade, A.A., & Pasyanos, M.E. (2006). Crustal thinning between the Ethiopian and East African plateaus from modeling Rayleigh wave dispersion. Geophys. Res. Lett., 33(13), L13301. https://doi.org/10.1029/2006GL025687

Beutel, E., Van Wijk, J., Ebinger, C., Keir, D., & Agostini, A. (2010). Formation and stability of magmatic segments in the Main Ethiopian and Afar rifts. Earth and Planetary Science Letters, 293(3-4), 225-235. https://doi.org/10.1016/j.epsl.2010.02.006

Boccaletti, S., Bragard, J., Arecchi, F.T., & Mancini, H. (1999). Synchronization in nonidentical extended systems. Physical Review Letters, 83(3), 536. https://doi.org/10.1103/PhysRevLett.83.536

Bonini, M., Corti, G., Innocenti, F., Manetti, P., Mazzarini, F., Abebe, T., Pecskay, Z. (2005). Evolution of the Main Ethiopian Rift in the frame of Afar and Kenya rifts propagation. Tectonics, 24, TC1007. https://doi.org/10.1029/2004TC001680

Bosworth W. (1992). Mesozoic and Early Tertiary rift tectonics in East Africa. Tectonophysics, 209, 115- 137.

Bott, M.H.P. (1991). Ridge push and associated plate interior stress in normal and hot spot regions. Tectonophysics, 200(1-3), 17-32. https://doi.org/10.1016/0040-1951(91)90003-B

Brotzu, P., Morbidelli, L., Nicoletti, M., Piccirillo, E.M., & Traversa, G. (1984). Miocene to Quaternary volcanism in eastern Kenya: sequence and geochronology. Tectonophysics, 101(1-2), 75-86. https://doi.org/10.1016/0040-1951(84)90043-X

Brune, S. (2014). Evolution of stress and fault patterns in oblique rift systems: 3-D numerical lithospheric-scale experiments from rift to breakup. Geochem. Geophys. Geosystems, 15(8), 3392–3415. https://doi.org/10.1002/2014GC005446

Brune, S., Corti, G., Ranalli, G. (2017). Controls of inherited lithospheric heterogeneity on rift linkage: Numerical and analogue models of interaction between the Kenyan and Ethiopian rifts across the Turkana depression. Tectonics, 36(9), 1767-1786. https://doi.org/10.1002/2017TC004739

Buck, W.R. (1991). Modes of continental lithospheric extension. Journal of Geophysical Research: Solid Earth, 96(B12), 20161-20178. https://doi.org/10.1029/91JB01485

Buck, W.R. (2006). The role of magma in the development of the Afro-Arabian Rift System. In: Yirgu, G., Ebinger, C.J., Maguire, P.K.H. (Eds.), The Afar Volcanic Province within the East African Rift System. Geological Society, London, Special Publications, 259(1), 43-54. https://doi.org/10.1144/GSL.SO.2006.259.01.05.

Casagli, A., Frezzotti, M. L., Peccerillo, A., Tiepolo, M., & De Astis, G. (2017). (Garnet)-spinel peridotite xenoliths from Mega (Ethiopia): Evidence for rejuvenation and dynamic thinning of the lithosphere beneath the southern Main Ethiopian Rift. Chemical Geology, 455, 231-248. https://doi.org/10.1016/j.chemgeo.2016.11.001

Casey, M., Ebinger, C., Keir, D., Gloaguen, R., & Mohamed, F. (2006). Strain accommodation in transitional rifts: Extension by magma intrusion and faulting in Ethiopian rift magmatic segments. Geological Society, London, Special Publications, 259(1), 143-163. https://doi.org/10.1144/GSL.SP.2006.259.01.13

Charsley, T.J. (1988). Geological Map of Kenya—Degree sheet 12, North Horr (scale 1:250,000). Government of Kenya, Ministry of Environment and Natural Resources, Mines and Geological Department, Nairobi, Kenya.

Chorowicz, J. (2005). The East African Rift System. Journal of African Earth Sciences, 43(1-3), 379–410. https://doi.org/10.1016/j.jafrearsci.2005.07.019

Conticelli, S., Sintoni, M. F., Abebe, T., Mazzarini, F., & Manetti, P. (1999). Petrology and geochemistry of ultramafic xenoliths and host lavas from the Ethiopian Volcanic Province: An insight into the upper mantle under eastern Africa. Acta Vulcanologica, 11(1), 143-160.

Corti, G., Bonini, M., Sokoutis, D., Innocenti, F., Manetti, P., Cloetingh, S., & Mulugeta, G. (2004). Continental rift architecture and patterns of magma migration: A dynamic analysis based on centrifuge models. Tectonics, 23(2). https://doi.org/10.1029/2003TC001561

Corti, G. (2008). Control of rift obliquity on the evolution and segmentation of the main Ethiopian rift. Nature Geoscience, 1, 258-262. https://doi.org/10.1038/ngeo160

Corti, G. (2009). Continental rift evolution: from rift initiation to incipient break-up in the Main Ethiopian Rift, East Africa. Earth-Science Reviews, 96(1-2), 1-53. https://doi.org/10.1016/j.earscirev.2009.06.005

Corti, G., Cioni, R., Franceschini, Z., Sani, F., Scaillet, S., Molin, P., Isola, I., Mazzarini, F., Brune, S., Keir, D., Erbello, A., Muluneh, A., Illsley-Kemp, F., Glerum, A. (2019). Aborted propagation of the Ethiopian rift caused by linkage with the Kenyan rift. Nature communications, 10, 1309. https://doi.org/10.1038/s41467-019-09335-2

DeMets, C., & Merkouriev, S. (2016). High-resolution estimates of Nubia–Somalia plate motion since 20 Ma from reconstructions of the Southwest Indian Ridge, Red Sea and Gulf of Aden. Geophysical Journal International, 207(1), 317–332. https://doi.org/10.1093/gji/ggw276

De Silva, S., & Lindsay, J.M. (2015). Chapter 15 - Primary volcanic landforms. In: Sigurdsson, H. (Ed.), The Encyclopedia of Volcanoes (Second Edition). Amsterdam, Academic Press, pp. 273-297. http://dx.doi.org/10.1016/B978-0-12-385938-9.00015-8.

Ebinger, C.J., Yemane, T., Harding, D.J., Tesfaye, S., Kelley, S., & Rex, D.C. (2000). Rift deflection, migration, and propagation: Linkage of the Ethiopian and Eastern rifts, Africa. GSA Bull., 112(2), 163–176. https://doi.org/10.1130/0016-7606(2000)112<163:RDMAPL>2.0.CO;2

Ebinger, C.J., & Casey, M. (2001). Continental breakup in magmatic provinces: An Ethiopian example. Geology, 29(6), 527-530. https://doi.org/10.1130/0091-7613(2001)029<0527:CBIMPA>2.0.CO;2

Emishaw, L., & Abdelsalam, M.G. (2019). Development of late Jurassic–early Paleogene and Neogene- Quaternary rifts within the Turkana Depression, East Africa from Satellite Gravity Data. Tectonics, 38(7), 2358-2377. https://doi.org/10.1029/2018TC005389

Erbello, A., & Kidane, T. (2018). Timing of volcanism and initiation of rifting in the Omo-Turkana depression, southwest Ethiopia: Evidence from paleomagnetism. Journal of African Earth Sciences, 139, 319-329. https://doi.org/10.1016/j.jafrearsci.2017.12.031

Fleitout, L., & Froidevaux, C. (1982). Tectonics and topography for a lithosphere containing density heterogeneities. Tectonics, 1(1), 21-56. https://doi.org/10.1029/TC001i001p00021

Fontijn, K., McNamara, K., Tadesse, A.Z., Pyle, D.M., Dessalegn, F., Hutchison, W., Mather, T.A., & Yirgu, G. (2018). Contrasting styles of post-caldera volcanism along the Main Ethiopian Rift: Implications for contemporary volcanic hazards. Journal of Volcanology and Geothermal Research, 356, 90-113. https://doi.org/10.1016/j.jvolgeores.2018.02.001

Fornaciai, A., Favalli, M., Karátson, D., Tarquini, S., & Boschi, E. (2012). Morphometry of scoria cones, and their relation to geodynamic setting: a DEM-based analysis. Journal of Volcanology and Geothermal Research, 217-218, 56-72. https://doi.org/10.1016/j.jvolgeores.2011.12.012

Foster, D.A., & Gleadow, A.J. (1996). Structural framework and denudation history of the flanks of the Kenya and Anza Rifts, East Africa. Tectonics, 15(2), 258-271. https://doi.org/10.1029/95TC02744

Gómez-Vasconcelos, M.G., Luis Macías, J., Avellán, D.R., Sosa-Ceballos, G., Garduño-Monroy, V.H., Cisneros-Máximo, G., ... & Perton, M. (2020). The control of preexisting faults on the distribution, morphology, and volume of monogenetic volcanism in the Michoacán-Guanajuato Volcanic Field. GSA Bull. https://doi.org/10.1130/B35397.1

Graettinger, A.H. (2018). Trends in maar crater size and shape using the global Maar Volcano Location and Shape (MaarVLS) database. Journal of Volcanology and Geothermal Research, 357, 1-13. https://doi.org/10.1016/j.jvolgeores.2018.04.002

Haag, M.B., Baez, W.A., Sommer, C.A., Arnosio, J.M., & Filipovich, R.E. (2019). Geomorphology and spatial distribution of monogenetic volcanoes in the southern Puna Plateau (NW Argentina). Geomorphology, 342, 196-209. https://doi.org/10.1016/j.geomorph.2019.06.008

Hackman, B.D., Charsley, T.J., Key, R.M., & Wilkinson, A.F. (1990). The development of the East African Rift system in north-central Kenya. Tectonophysics, 184(2), 189-211. https://doi.org/10.1016/0040-1951(90)90053-B

Hayward, N.J., Ebinger, C.J. (1996). Variations in the along-axis segmentation of the Afar Rift system. Tectonics, 15(2), 244-257. https://doi.org/10.1029/95TC02292

Hunt, J.A., Mather, T.A., Pyle, D.M. (2020). Morphological comparison of distributed volcanic fields in the Main Ethiopian Rift using high-resolution digital elevation models. Journal of Volcanology and Geothermal Research 393, 106732. https://doi.org/10.1016/j.jvolgeores.2019.106732

Hutchison, W., Mather, T.A., Pyle, D.M., Biggs, J., & Yirgu, G. (2015). Structural controls on fluid pathways in an active rift system: A case study of the Aluto volcanic complex. Geosphere, 11(3), 542–562. https://doi.org/10.1130/GES01119.1

Hutchison, W., Fusillo, R., Pyle, D.M., Mather, T. A., Blundy, J.D., Biggs, J., ... & Calvert, A.T. (2016). A pulse of mid-Pleistocene rift volcanism in Ethiopia at the dawn of modern humans. Nature communications, 7, 13192. https://doi.org/10.1038/ncomms13192

Iaffaldano, G., Hawkins, R., & Sambridge, M. (2014). Bayesian noise-reduction in Arabia/Somalia and Nubia/Arabia finite rotations since ~20 Ma: Implications for Nubia/Somalia relative motion. Geochem. Geophys. Geosystems, 15(4), 845–854. https://doi.org/10.1002/2013GC005089

Irvine T.N., & Baragar W.R.A. (1971). A Guide to the Chemical Classification of the Common Volcanic Rocks. Canadian Journal of Earth Sciences, 8(5), 523-548. https://doi.org/10.1139/e71-055.

Isola, I., Mazzarini, F., Corti, G., Bonini, M. (2014). Spatial variability of volcanic features in early-stage rift settings: the case of the Tanzania divergence, East African rift system. Terra Nova, 26(6), 461–468. https://doi.org/10.1111/ter.12121.

Jaimes-Viera, M.C., Del Pozzo, A.M., Layer, P.W., Benowitz, J.A., & Nieto-Torres, A. (2018). Timing the evolution of a monogenetic volcanic field: Sierra Chichinautzin, Central Mexico. Journal of Volcanology and Geothermal Research, 356, 225-242. https://doi.org/10.1016/j.jvolgeores.2018.03.013

Keir, D., Bastow, I.D., Corti, G., Mazzarini, F., Rooney, T.O. (2015). The origin of along-rift variations in faulting and magmatism in the Ethiopian rift. Tectonics, 34(3), 464-477. https://doi.org/10.1002/2014TC003698

Kereszturi, G., & Németh, K. (2012). Monogenetic basaltic volcanoes: genetic classification, growth, geomorphology and degradation. In: Németh, K. (Ed.), Updates in Volcanology - New Advances in Understanding Volcanic Systems. Rijeka, Croatia, inTech Open, 3-88, https://dx.doi.org/10.5772/51387.

Kereszturi, G., Németh, K., Cronin, S. J., Agustín-Flores, J., Smith, I.E., & Lindsay, J. (2013). A model for calculating eruptive volumes for monogenetic volcanoes—Implication for the Quaternary Auckland Volcanic Field, New Zealand. Journal of Volcanology and Geothermal Research, 266, 16-33. https://dx.doi.org/10.1016/j.jvolgeores.2013.09.003

Kervyn, M., Ernst, G.G.J., Carracedo, J.C., Jacobs, P. (2012). Geomorphometric variability of "monogenetic" volcanic cones: Evidence from Mauna Kea, Lanzarote and experimental cones. Geomorphology 136(1), 59–75. https://doi.org/10.1016/j.geomorph.2011.04.009

Kurz, T., Gloaguen, R., Ebinger, C., Casey, M., Abebe, B. (2007). Deformation distribution and type in the Main Ethiopian Rift (MER): a remote sensing study. Journal of African Earth Sciences 48, 100–114. https://doi.org/10.1016/j.jafrearsci.2006.10.008

Le Corvec, N., Spörli, K.B., Rowland, J., Lindsay, J., 2013. Spatial distribution and alignments of volcanic centers: Clues to the formation of monogenetic volcanic fields. Earth-Science Reviews 124, 96–114, doi:10.1016/j.earscirev.2013.05.005.

Le Maitre, R.W., Streckeisen, A., Zanettin, B., Le Bas, M.J., Bonin, B., & Bateman, P. (Eds.). (2002). Igneous rocks: a classification and glossary of terms: recommendations of the International Union of Geological Sciences Subcommission on the Systematics of Igneous Rocks. Cambridge University Press, 30-39.

Lloyd, R., Biggs, J., Birhanu, Y., Wilks, M., Kendall, J., Ayele, A., & Lewi, E. (2018). Sustained Uplift at a Continental Rift Caldera. Journal of Geophysical Research B: Solid Earth, 123(6), 5209–5226. https://doi.org/10.1029/2018JB015711

Lorenz, V., Suhr, P., & Suhr, S. (2017). Phreatomagmatic maar-diatreme volcanoes and their incremental growth: a model. Geological Society, London, Special Publications, 446(1), 29-59. https://doi.org/10.1144/SP446.4

Martin-Jones, C.M., Lane, C.S., Pearce, N.J.G., Smith, V.C., Lamb, H.F., Schaebitz, F., Viehberg, F., Brown, M.C., Frank, U., & Asrat, A. (2017). Recurrent explosive eruptions from a high-risk Main Ethiopian Rift volcano throughout the Holocene. Geology, 45(12), 1127–1130. https://doi.org/10.1130/G39594.1

Mazzarini, F., & D'Orazio, M. (2003). Spatial distribution of cones and satellite-detected lineaments in the Pali Aike Volcanic Field (southernmost Patagonia): insights into the tectonic setting of a Neogene rift system. Journal of Volcanology and Geothermal Research, 125(3-4), 291-305. https://doi.org/10.1016/S0377-0273(03)00120-3

Mazzarini, F., & Isola, I. (2010). Monogenetic vent self-similar clustering in extending continental crust: Examples from the East African Rift System. Geosphere, 6(5), 567-582. https://doi.org/10.1130/GES00569.1

Mazzarini, F., Le Corvec, N., Isola, I., Favalli, M. (2016). Volcanic field elongation, vent distribution, and tectonic evolution of a continental rift: The Main Ethiopian Rift example. Geosphere, 12(3), 706–720. https://doi.org/10.1130/GES01193.1

McNamara, K., Cashman, K.V., Rust, A.C., Fontijn, K., Chalié, F., Tomlinson, E.L., & Yirgu, G. (2018). Using Lake Sediment Cores to Improve Records of Volcanism at Aluto Volcano in the Main Ethiopian Rift. Geochemistry, Geophysics, Geosystems, 19(9), 3164–3188. https://doi.org/10.1029/2018GC007686

Morley, C.K., Wescott, W.A., Stone, D.M., Harper, R.M., Wigger, S.T., & Karanja, F.M. (1992). Tectonic evolution of the northern Kenyan Rift. Journal of the Geological Society, 149(3), 333-348. https://doi.org/10.1144/gsjgs.149.3.0333

Morley, C.K., Wescott, W.A., Stone, D.M., Harper, R.M., Wigger, S.T., Day, R.A., & Karanja, F.M. (1999). Chapter 2 - Geology and Geophysics of the Western Turkana Basins, Kenya. In: Morley, C.K. (Ed.), Geoscience of Rift Systems—Evolution of East Africa: AAPG Studies in Geology No. 44, p. 19–54.

Muirhead, J.D., Kattenhorn, S.A., & Le Corvec, N. (2015). Varying styles of magmatic strain accommodation across the East African Rift. Geochemistry, Geophysics, Geosystems, 16(8), 2775-2795. https://doi.org/10.1002/2015GC005918

Németh, K., Risso, C., Nullo, F., & Kereszturi, G. (2011). The role of collapsing and cone rafting on eruption style changes and final cone morphology: Los Morados scoria cone, Mendoza, Argentina. Central European Journal of Geosciences, 3(2), 102-118. https://doi.org/10.2478/s13533-011-0008-4.

Németh, K., & Kereszturi, G. 2015. Monogenetic volcanism: personal views and discussion. International Journal of Earth Sciences 104(8): 2131-2146. https://doi.org/10.1007/s00531-015-1243-6

Orlando, A., Abebe, T., Manetti, P., Santo, A.P., Corti, G. (2006). Petrology of mantle xenoliths from Megado and Dilo, Kenya rift, southern Ethiopia. Ofioliti, 31(2), 71-87.

Paez, F.J.D. (2006). Study of the erosion of the monogenic basalt volcanoes of El Cerrillar, Guamasa and Enmedio, in Teide National Park (Tenerife. Canaries. Spain). Boletin De La Asociacion De Geografos Espanoles(42): 285-301.

Paez, J.D. (2010). The cinder cones of Tenerife (Canary Islands, Spain): implications for volcanic hazard and volcanic risk. Scripta Nova-Revista Electronica de Geografia y Ciencias Sociales 14(324).

Pinkerton, H., & Wilson, L. (1994). Factors controlling the lengths of channel-fed lava flows. Bulletin of Volcanology, 56(2), 108-120. https://doi.org/10.1007/BF00304106

Pioli, L., Erlund, E., Johnson, E., Cashman, K., Wallace, P., Rosi, M., & Delgado Granados, H., 2008. Explosive dynamics of violent Strombolian eruptions: The eruption of Parícutin Volcano 1943–1952 (Mexico). Earth and Planetary Science Letters 271, 359–368. https://doi:10.1016/j.epsl.2008.04.026

Porter, S.C. (1972). Distribution, morphology and size frequency of cinder cones on Mauna Kea Volcano, Hawaii. GSA Bull., 83(12), 3607-3612. https://doi.org/10.1130/0016-7606(1972)83[3607:DMASFO]2.0.CO;2

Rooney, T.O. (2010). Geochemical evidence of lithospheric thinning in the southern Main Ethiopian Rift. Lithos, 117(1-4), 33-48.

Rooney, T.O., Bastow, I.D., & Keir, D. (2011). Insights into extensional processes during magma assisted rifting: Evidence from aligned scoria cones. Journal of Volcanology and Geothermal Research, 201(1-4), 83-96. https://doi.org/10.1016/j.jvolgeores.2010.07.019

Saria, E., Calais, E., Stamps, D.S., Delvaux, D., Hartnady, C.J.H. (2014). Present-day kinematics of the East African Rift. J. Geophys. Res.: Solid Earth, 119(4), 3584–3600. https://doi.org/10.1002/2013JB010901

Saucedo, R., Macías, J.L., Ocampo-Díaz, Y.Z.E., Gómez-Villa, W., Rivera-Olguín, E., Castro-Govea, R., ... & Carrasco-Núñez, G. (2017). Mixed magmatic–phreatomagmatic explosions during the formation of the Joya Honda maar, San Luis Potosí, Mexico. Geological Society, London, Special Publications, *446*(1), 255-279. https://doi.org/10.1144/SP446.11

Scaillet, S. (2000). Numerical error analysis in $^{40}Ar/^{39}Ar$ dating. Chemical Geology.; 162(3-4), 269–298. https://doi.org/10.1016/S0009-2541(99)00149-7

Scaillet, S., Rotolo, S.G., La Felice, S., Vita-Scaillet, G. (2011). High-resolution $^{40}Ar/^{39}Ar$ chronostratigraphy of the post-caldera (<20 ka) volcanic activity at Pantelleria, Sicily Strait. Earth Planet. Sci. Lett., 309(3-4), 280-290. https://doi.org/10.1016/j.epsl.2011.07.009

Shillington, D.J., Scott, C.L., Minshull, T.A., Edwards, R.A., Brown, P.J., & White, N. (2009). Abrupt transition from magma-starved to magma-rich rifting in the eastern Black Sea. Geology, 37(1), 7–10. https://doi.org/10.1130/G25302A.1

Shinjo, R., Chekol, T., Meshesha, D., Itaya, T., Tatsumi, T. (2011). Geochemistry and geochronology of the mafic lavas from the southeastern Ethiopian rift (the East African Rift System): assessment of models on magma sources, plume–lithosphere interaction and plume evolution. Contrib Mineral Petrol, 162, 209–230. https://doi.org/10.1007/s00410-010-0591-2

Siegburg, M., Gernon, T.M., Bull, J.M., Keir, D., Barfod, D.N., Taylor, R.N., Abebe, B., & Ayele, A. (2017). Geological evolution of the Boset-Bericha Volcanic Complex, Main Ethiopian

Rift: 40Ar/39Ar evidence for episodic Pleistocene to Holocene volcanism. Journal of Volcanology and Geothermal Research, 351, 115–133. https://doi.org/10.1016/j.jvolgeores.2017.12.014

Sippel, J., Meeßen, C., Cacace, M., Mechie, J., Fishwick, S., Heine, C., Scheck-Wenderoth, M., & Strecker, M.R. (2017). The Kenya rift revisited: insights into lithospheric strength through data-driven 3-D gravity and thermal modelling. Solid Earth, 8(1), 45–81, doi:10.5194/se-8-45-2017.

Spera, F.J. (1980). Chapter 7 - Aspects of magma transport. In: Hargraves, R.B. (Ed.), Physics of magmatic processes. Princeton University Press, Princeton, New Jersey, pp. 265-315.

Strecker, M.R., & Bosworth, W. (1997). Stress field changes in the Africo-Arabian rift system during the Miocene to Recent period. Tectonophysics, 278(1-4), 47-72. https://doi.org/10.1016/S0040-1951(97)00094-2

Tadesse, A.Z., Ayalew, D., Pik, R., Yirgu, G., & Fontijn, K. (2018). Magmatic evolution of the Boku Volcanic Complex, Main Ethiopian Rift. Journal of African Earth Sciences, 149, 109–130. https://doi.org/10.1016/j.jafrearsci.2018.08.003

Turcotte, D.L., & Schubert, G. (2002). Geodynamics, 2nd edn Cambridge University Press. Cambridge, UK, 456.

Vetel, W., & Le Gall, B. (2006). Dynamics of prolonged continental extension in magmatic rifts: the Turkana Rift case study (North Kenya). Geol. Soc. Lond. Spec. Publ., 259(1), 209–233. https://doi.org/10.1144/GSL.SP.2006.259.01.17

Wadge, G., Biggs, J., Lloyd, R., & Kendall, J.M. (2016). Historical volcanism and the state of stress in the East African Rift System. Frontiers in Earth Science, 4, 86. https://doi.org/10.3389/feart.2016.00086

Watkins, R.T. (1983). The geology of the Suregei-Asille District and the Upper Bakate Valley, northern Kenya. PhD thesis, Univ. of London, London.

White, R., & McKenzie, D. (1989). Magmatism at rift zones: The generation of volcanic continental margins and flood basalts. Journal of Geophysical Research, 94(B6), 7685–7729. https://doi.org/10.1029/JB094iB06p07685

White, R.S., Smith, L.K., Roberts, A.W., Christie, P.A.F., Kusznir, N.J., and the rest of the iSIMM Team (2008). Lower-crustal intrusion on the North Atlantic continental margin. Nature, 452, 460–464. https://doi.org/10.1038/nature06687

White, S.M., Crisp, J.A., & Spera, F.J. (2006). Long- term volumetric eruption rates and magma budgets. Geochem. Geophys. Geosyst., 7(3). https://doi.org/10.1029/2005GC001002

White, J.D.L., & Ross, P.S. (2011). Maar-diatreme volcanoes: A review. Journal of Volcanology and Geothermal Research, 201(1-4), 1–29. https://doi.org/10.1016/j.jvolgeores.2011.01.010

Wilson, M.J. (2007). Igneous Petrogenesis – A global tectonic approach. Springer, p. 465.

Woldetinsae, G., & Götze, H.J. (2005). Gravity field and isostatic state of Ethiopia and adjacent areas. J. Afr. Earth Sci., 41(1–2), 103–117. https://doi.org/10.1016/j.jafrearsci.2005.02.004

Wood, C.A. (1980). Morphometric analysis of cinder cone degradation. Journal of Volcanology and Geothermal Research, 8(2-4), 137-160.

Wright, T.J., Sigmundsson, F., Pagli, C., Belachew, M., Hamling, I.J., Brandsdóttir, B., ... & Einarsson, P. (2012). Geophysical constraints on the dynamics of spreading centres from rifting episodes on land. Nature Geoscience, 5(4), 242-250. https://doi.org/10.1038/ngeo1428

Table 1. Number of cones (C), maars (M) and tuff rings (TR), considering the number of identified vents in each volcanic field (VF). *Note that the real number of cones is actually much higher considering that all the vents which were not considered form morphometric analysis are most likely cones.

VF	Total vents identified	Vents used for morphometric analysis	C*	M	TR
Dilo	52	26	9	14	3
Mega	114	41	33	8	0

Table 2. Summary table reporting the twelve analysed samples. MDZ03 to MDZ13 belong to Dilo VF; MDZ17 to MDZ33 belong to Mega VF.

Irrad. #	Rock type	Phase	Name	Run #	Plateau age (Ma) ± 1σ	MSWD/(n-1) LwB		UpB	n	N	Total gas age (Ma) ± 1σ	Irradiated mass (mg)	wt.% K_2O	Reference
#6-A(AA)	basalt	Gdm	MDZ-03	N101.MS1	0.153 ± 0.006	0.53	1.09	1.59	20	25	0.169 ± 0.008	113.149	2.48	Corti et al. (2019)
#6-A(AB)	basalt	Gdm	MDZ-05	N97.MS1	3.686 ± 0.014	0.39	1.07	1.83	11	24	3.799 ± 0.041	223.259	1.07	Corti et al. (2019)
#6-A(AC)	basalt	Gdm	MDZ-06	N104.MS1	0.324 ± 0.012	0.39	1.64	1.83	11	30	0.522 ± 0.011	169.990	2.04	this study
#6-A(AD)	basalt	Gdm	MDZ-10	N100.MS1	0.134 ± 0.004	0.55	1.57	1.56	22	22	0.136 ± 0.004	194.148	unknown	Corti et al. (2019)
#6-A(AE)	basalt	Gdm	MDZ-12	N103.MS1	3.749 ± 0.030	0.42	1.45	1.79	12	28	3.850 ± 0.044	107.426	1.02	Corti et al. (2019)
#6-A(AF)	basalt	Gdm	MDZ-13	N99.MS1	0.164 ± 0.007	0.54	0.74	1.57	21	22	0.204 ± 0.012	43.091	1.83	Corti et al. (2019)
#6-A(AG)	basalt	Gdm	MDZ-17	N107.MS1	0.116 ± 0.005	0.39	1.91	1.83	11	17	0.300 ± 0.006	198.314	1.37	this study
#6-A(AH)	basalt	Gdm	MDZ-20	N109.MS1	-0.004 ± 0.006	0.42	1.06	1.79	12	18	0.009 ± 0.005	135.572	1.51	this study
#6-A(AI)	basalt	Gdm	MDZ-21	N106.MS1	0.048 ± 0.006	0.27	1.92	2.1	7	18	0.039 ± 0.006	188.228	2.39	this study
#6-A(AJ)	basalt	Gdm	MDZ-27	N108.MS1	-0.087 ± 0.012	0.54	1.08	1.57	21	26	-0.020 ± 0.015	152.266	1.71	this study
#6-A(AL)	basalt	Gdm	MDZ-31	N105.MS1	-0.004 ± 0.006	0.48	1.63	1.67	16	18	0.043 ± 0.009	158.334	2.06	this study
#6-A(AM)	basalt	Gdm	MDZ-33	N98.MS1	-0.012 ± 0.008	0.51	1.42	1.62	18	21	-0.056 ± 0.050	208.682	2.36	this study

Author Statement

Zara Franceschini: Conceptualization, Methodology, Data curation, Writing- Original draft preparation, Visualization, Investigation, Writing- Reviewing and Editing
Raffaello Cioni, **Giacomo Corti**, **Federico Sani**, **Stéphane Scaillet**: Conceptualization, Methodology, Data curation, Visualization, Investigation, Writing- Reviewing and Editing
Ilaria Isola, **Francesco Mazzarini**: Methodology, Data curation, Visualization, Writing- Reviewing and Editing
Florian Duval: Methodology, Data curation
Asfaw Erbello, **Ameha Muluneh**: Investigation
Sascha Brune: Methodology, Visualization, Investigation, Writing- Reviewing and Editing

Declaration of interests

☒ The authors declare that they have no known competing financial interests or personal relationships that could have appeared to influence the work reported in this paper.

☐The authors declare the following financial interests/personal relationships which may be considered as potential competing interests:

Highlights:

1) Multidisciplinary study of the Dilo and Mega volcanic fields in South Ethiopia

2) Two phases of volcanism: Pliocene tholeiitic basalts and Quaternary alkaline basalts

3) Quaternary volcanism is unrelated to rifting and rift-related structures

4) Inherited fabrics and local stress field influence volcanism after rift abandonment

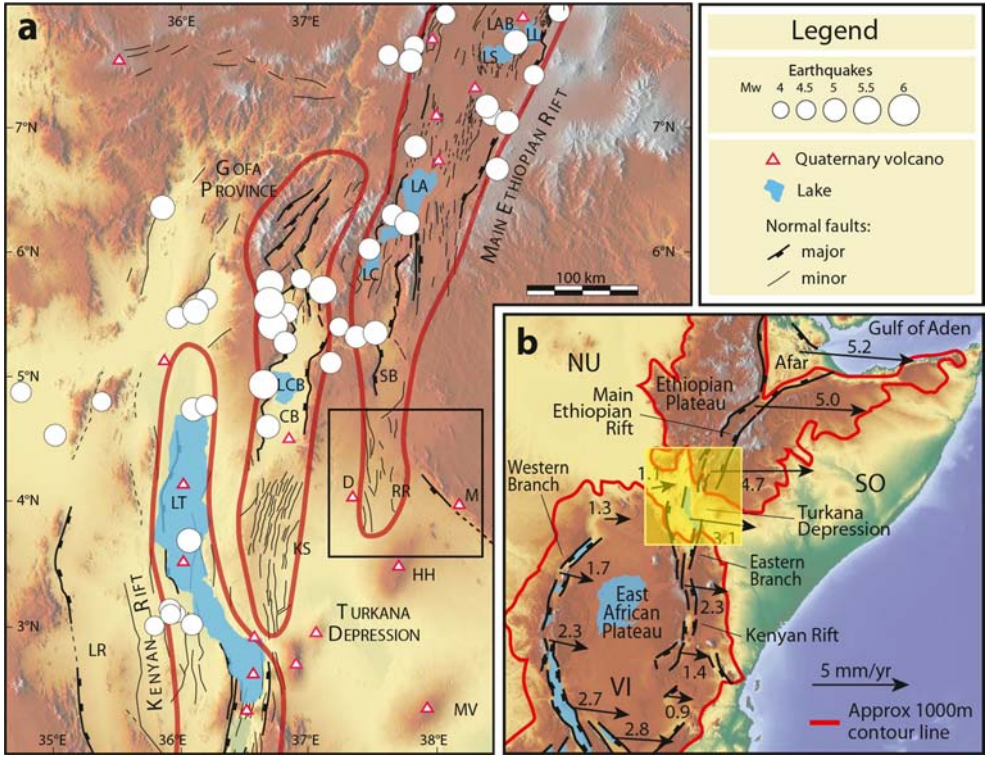
a
36°E
37°E
7°N
6°N
5°N
4°N
3°N
35°E
38°E
LAB
LS
LL
GOFA PROVINCE
LA
LC
MAIN ETHIOPIAN RIFT
100 km
LCB
CB
SB
D
RR
M
LT
KS
HH
TURKANA DEPRESSION
KENYAN RIFT
LR
MV
Legend
Earthquakes
Mw 4 4.5 5 5.5 6
Quaternary volcano
Lake
Normal faults:
major
minor
b
NU
Gulf of Aden
5.2
Afar
Ethiopian Plateau
Main Ethiopian Rift
5.0
Western Branch
1.1
4.7
SO
1.3
Turkana Depression
3.1
Eastern Branch
1.7
East African Plateau
2.3
2.3
Kenyan Rift
1.4
5 mm/yr
VI
2.7
0.9
2.8
Approx 1000m contour line

Figure 1

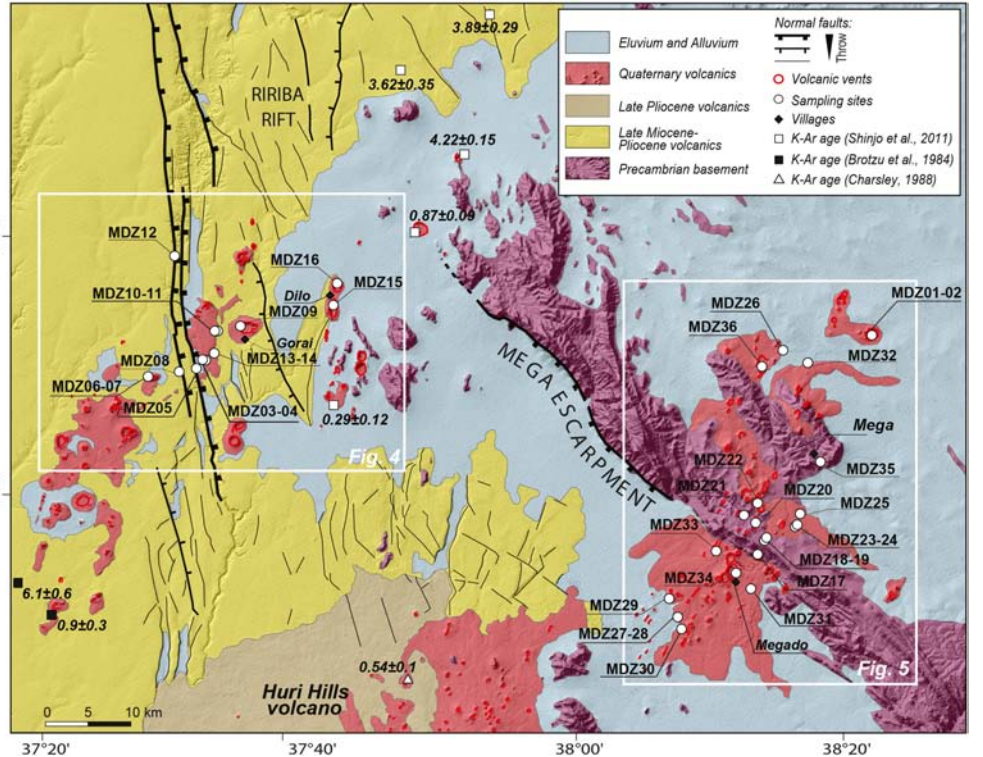
Eluvium and Alluvium
Quaternary volcanics
Late Pliocene volcanics
Late Miocene-Pliocene volcanics
Precambrian basement
Normal faults:
Throw
Volcanic vents
Sampling sites
Villages
K-Ar age (Shinjo et al., 2011)
K-Ar age (Brotzu et al., 1984)
K-Ar age (Charsley, 1988)
RIRIBA RIFT
MEGA ESCARPMENT
Huri Hills volcano
Dilo
Gorai
Mega
Megado
3.89±0.29
3.62±0.35
4.22±0.15
0.87±0.09
0.29±0.12
6.1±0.6
0.9±0.3
0.54±0.1
MDZ12
MDZ16
MDZ15
MDZ10-11
MDZ09
MDZ13-14
MDZ08
MDZ06-07
MDZ05
MDZ03-04
MDZ01-02
MDZ26
MDZ36
MDZ32
MDZ22
MDZ35
MDZ21
MDZ20
MDZ25
MDZ33
MDZ23-24
MDZ18-19
MDZ34
MDZ17
MDZ29
MDZ31
MDZ27-28
MDZ30
Fig. 4
Fig. 5
0 5 10 km
4°20'
4°00'
37°20'
37°40'
38°00'
38°20'

Figure 2

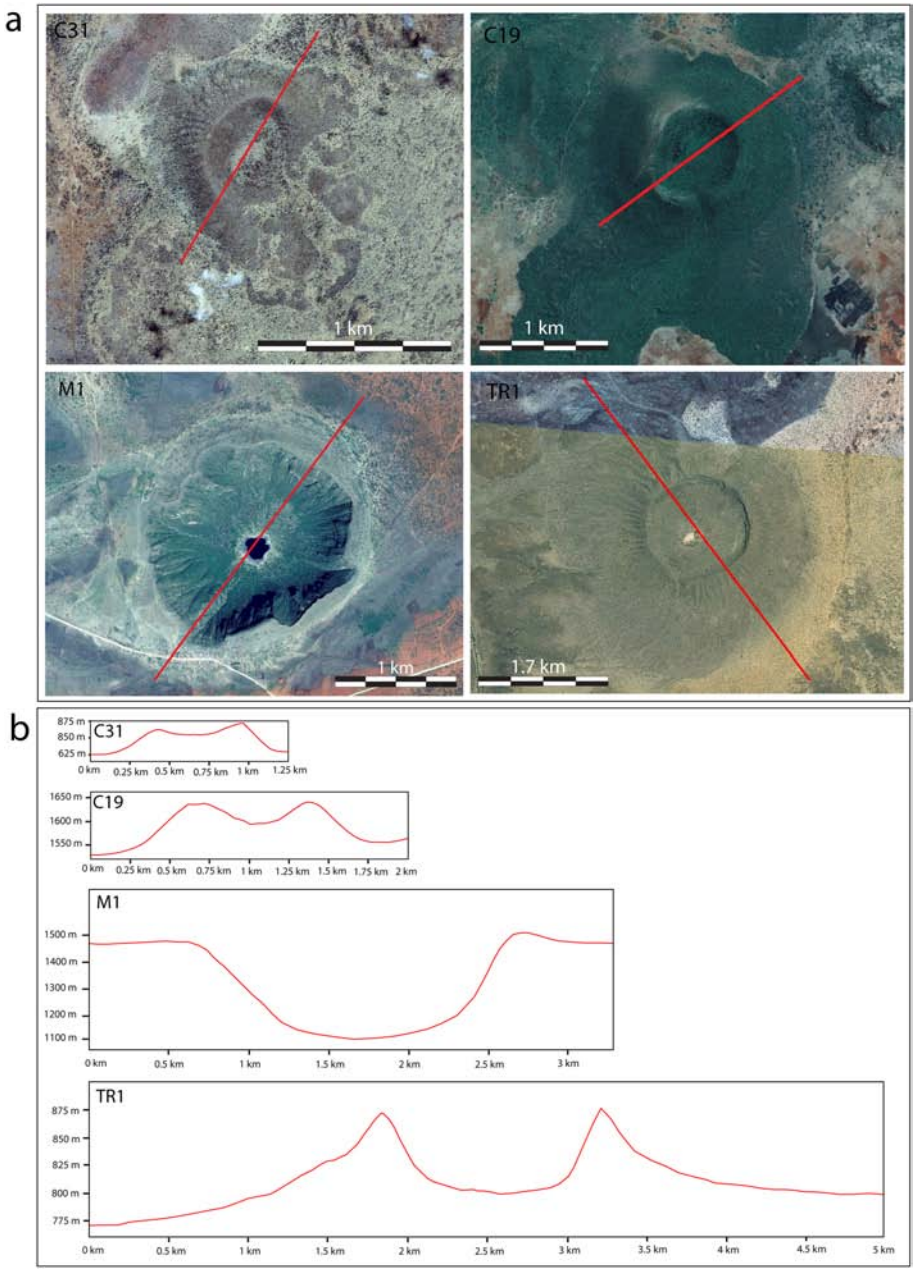
a
C31
1 km
C19
1 km
M1
1 km
TR1
1.7 km
b
C31
875 m
850 m
625 m
0 km
0.25 km
0.5 km
0.75 km
1 km
1.25 km
C19
1650 m
1600 m
1550 m
0 km
0.25 km
0.5 km
0.75 km
1 km
1.25 km
1.5 km
1.75 km
2 km
M1
1500 m
1400 m
1300 m
1200 m
1100 m
0 km
0.5 km
1 km
1.5 km
2 km
2.5 km
3 km
TR1
875 m
850 m
825 m
800 m
775 m
0 km
0.5 km
1 km
1.5 km
2 km
2.5 km
3 km
3.5 km
4 km
4.5 km
5 km

Figure 3

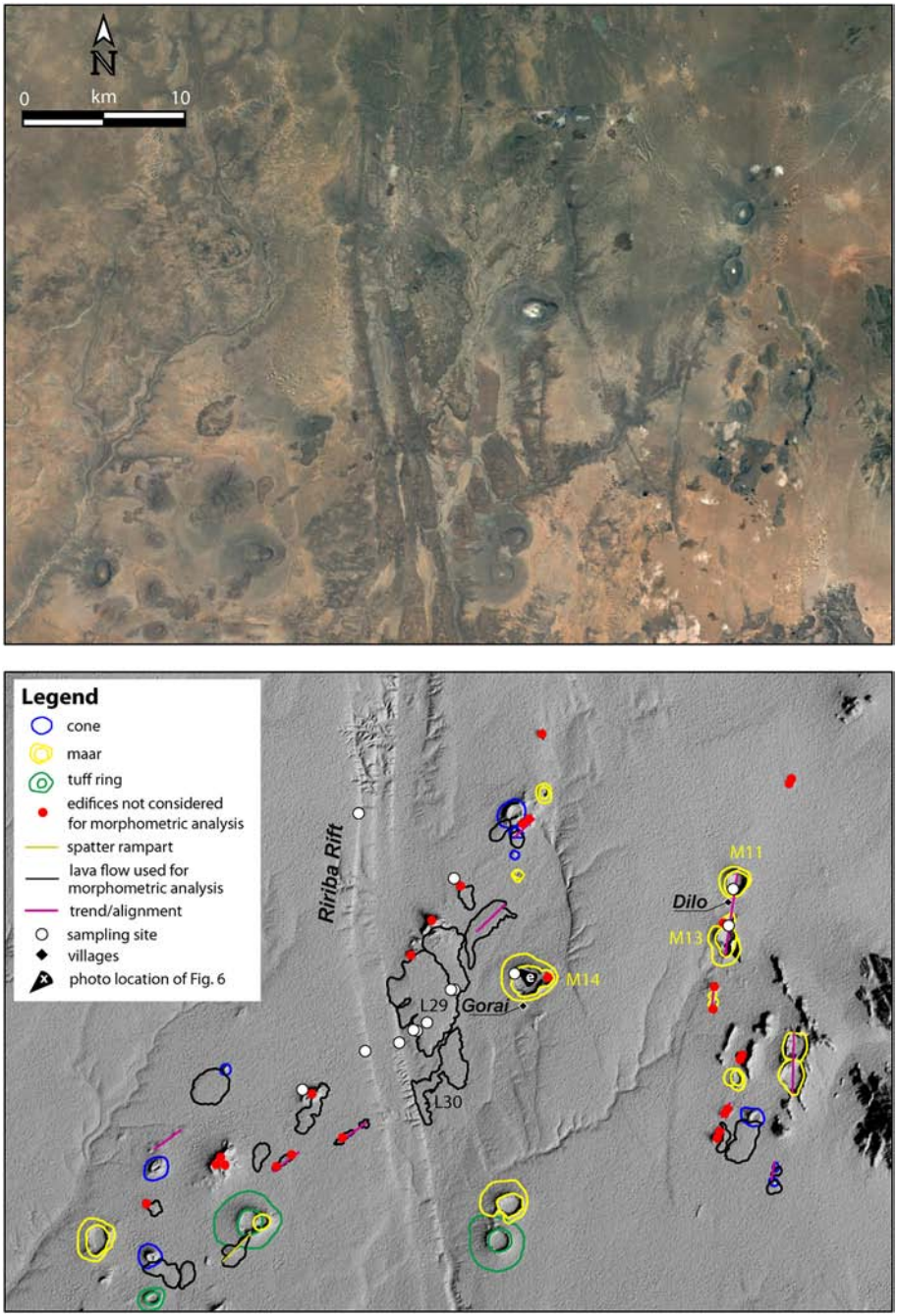
N
0
km
10
Legend
cone
maar
tuff ring
edifices not considered for morphometric analysis
spatter rampart
lava flow used for morphometric analysis
trend/alignment
sampling site
villages
photo location of Fig. 6
Ririba Rift
M11
Dilo
M13
M14
L29
Gorai
L30

Figure 4

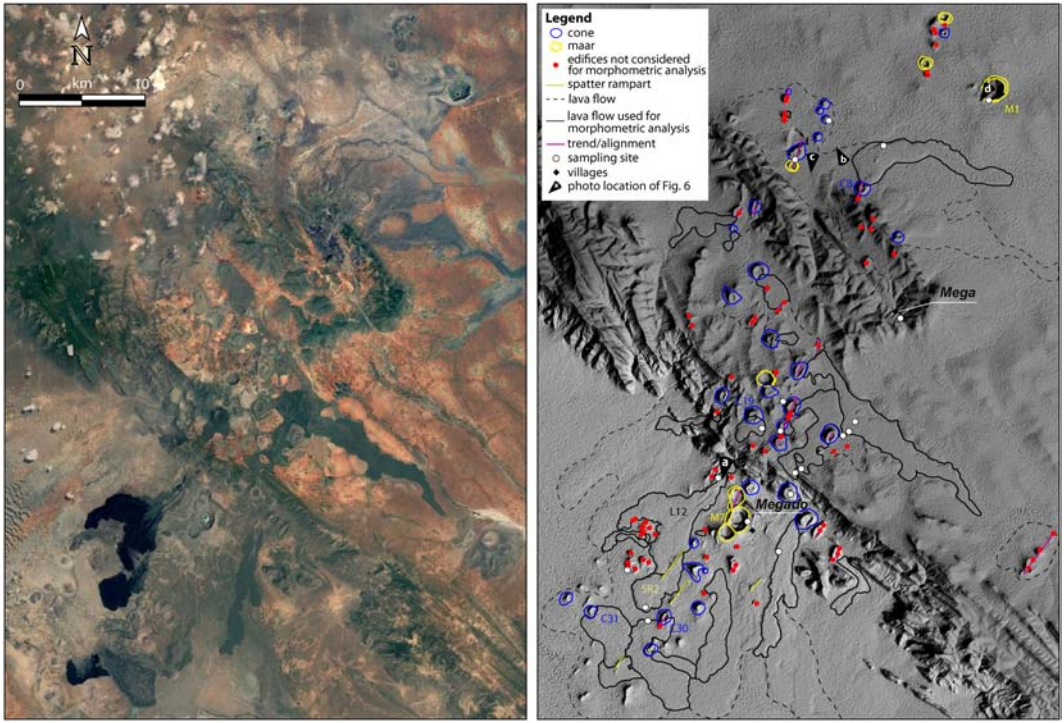
N
0
km
10
Legend
cone
maar
edifices not considered for morphometric analysis
spatter rampart
lava flow
lava flow used for morphometric analysis
trend/alignment
sampling site
villages
photo location of Fig. 6
Mega
Megadda
M1
L12
C31
F30

Figure 5

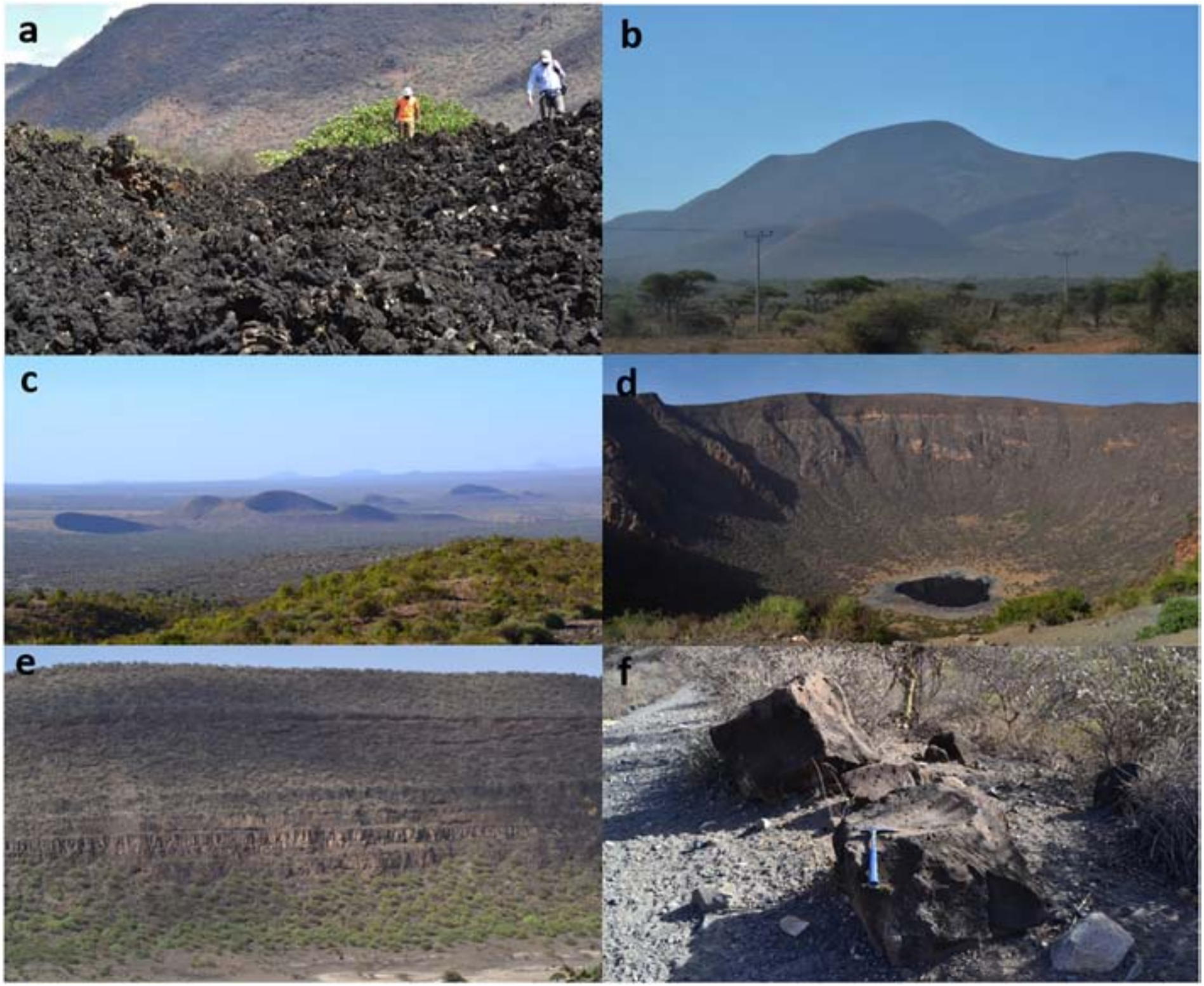

Figure 6

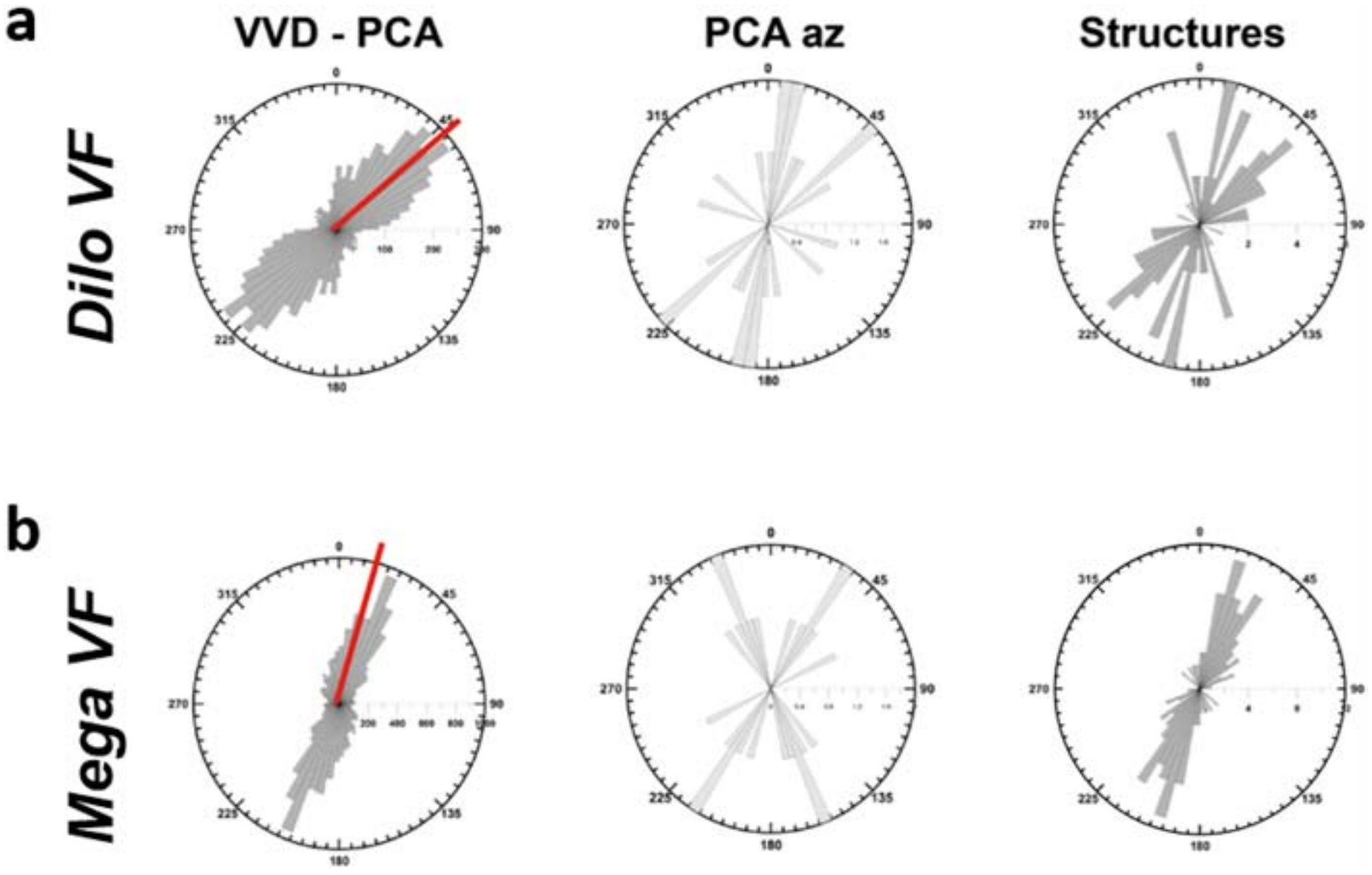
a
VVD - PCA
PCA az
Structures
Dilo VF
b
Mega VF
0
45
90
135
180
225
270
315

Figure 7

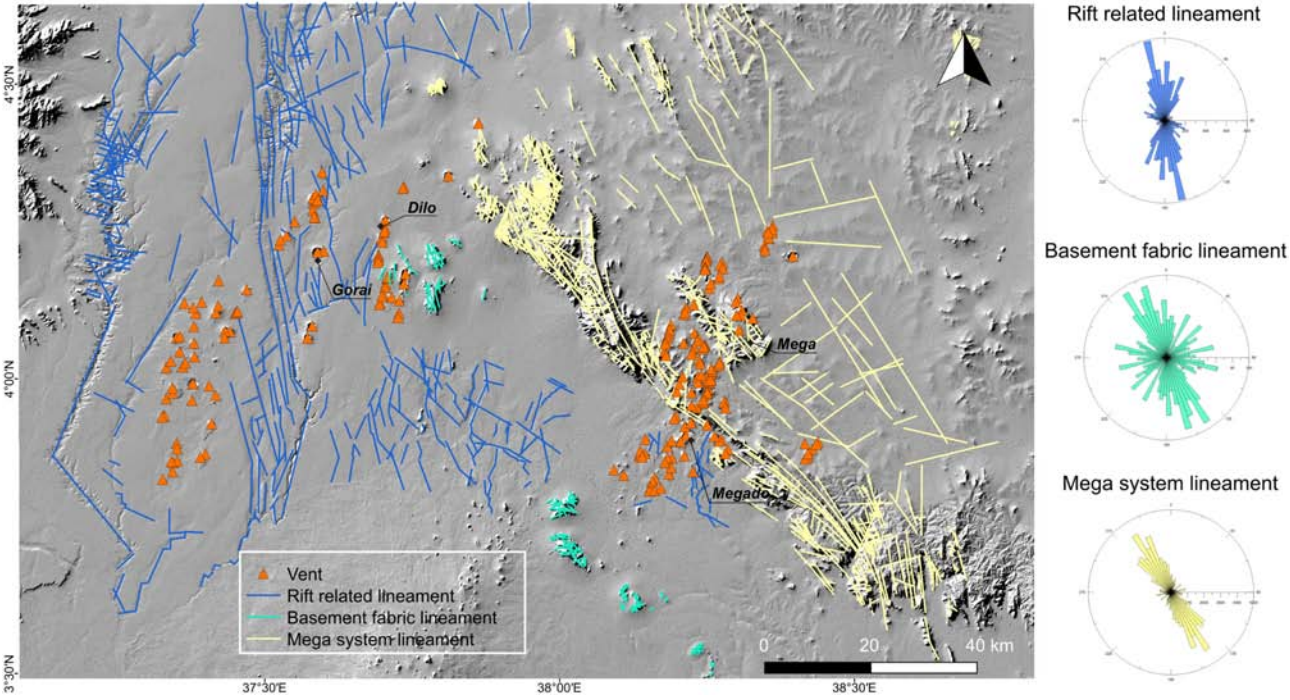
Rift related lineament
Basement fabric lineament
Mega system lineament
Dilo
Gorai
Mega
Megado
Vent
Rift related lineament
Basement fabric lineament
Mega system lineament
0
20
40 km
4°30'N
4°00'N
3°30'N
37°30'E
38°00'E
38°30'E

Figure 8

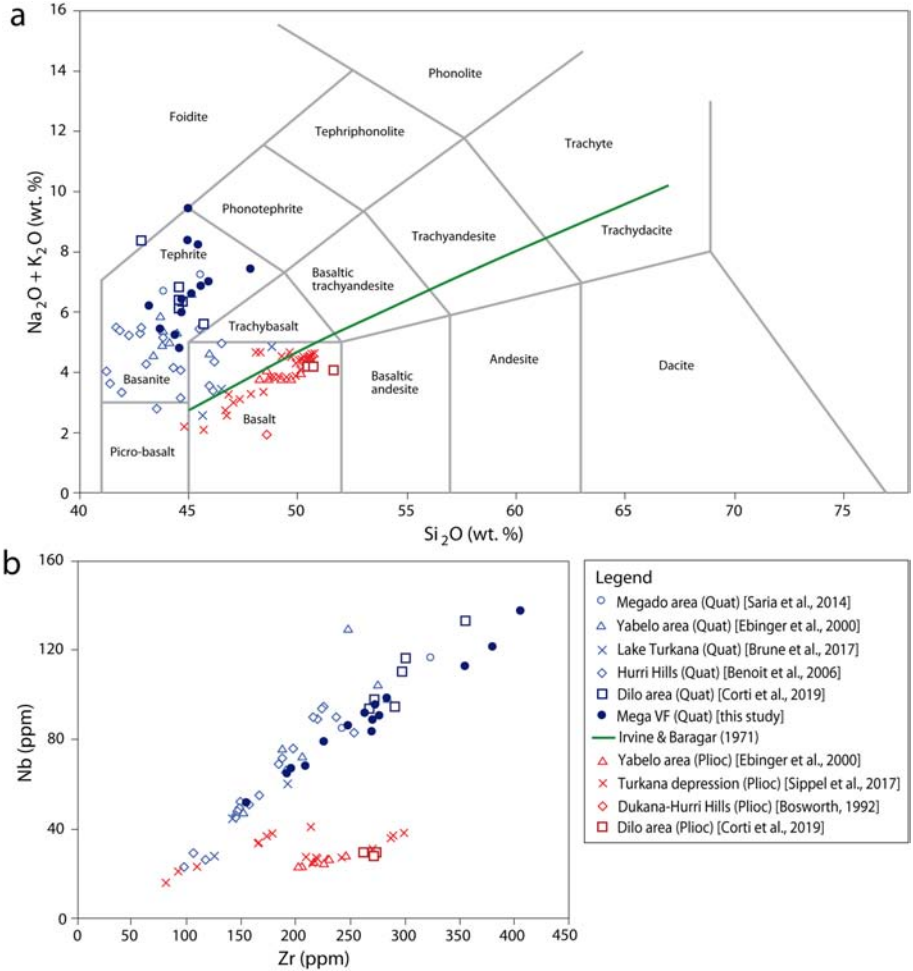
a
Foidite
Phonolite
Tephriphonolite
Trachyte
Phonotephrite
Trachyandesite
Trachydacite
Tephrite
Basaltic trachyandesite
Trachybasalt
Basanite
Basaltic andesite
Andesite
Dacite
Basalt
Picro-basalt
Na2O + K2O (wt. %)
Si2O (wt. %)
b
Nb (ppm)
Zr (ppm)
Legend
Megado area (Quat) [Saria et al., 2014]
Yabelo area (Quat) [Ebinger et al., 2000]
Lake Turkana (Quat) [Brune et al., 2017]
Hurri Hills (Quat) [Benoit et al., 2006]
Dilo area (Quat) [Corti et al., 2019]
Mega VF (Quat) [this study]
Irvine & Baragar (1971)
Yabelo area (Plioc) [Ebinger et al., 2000]
Turkana depression (Plioc) [Sippel et al., 2017]
Dukana-Hurri Hills (Plioc) [Bosworth, 1992]
Dilo area (Plioc) [Corti et al., 2019]

Figure 9

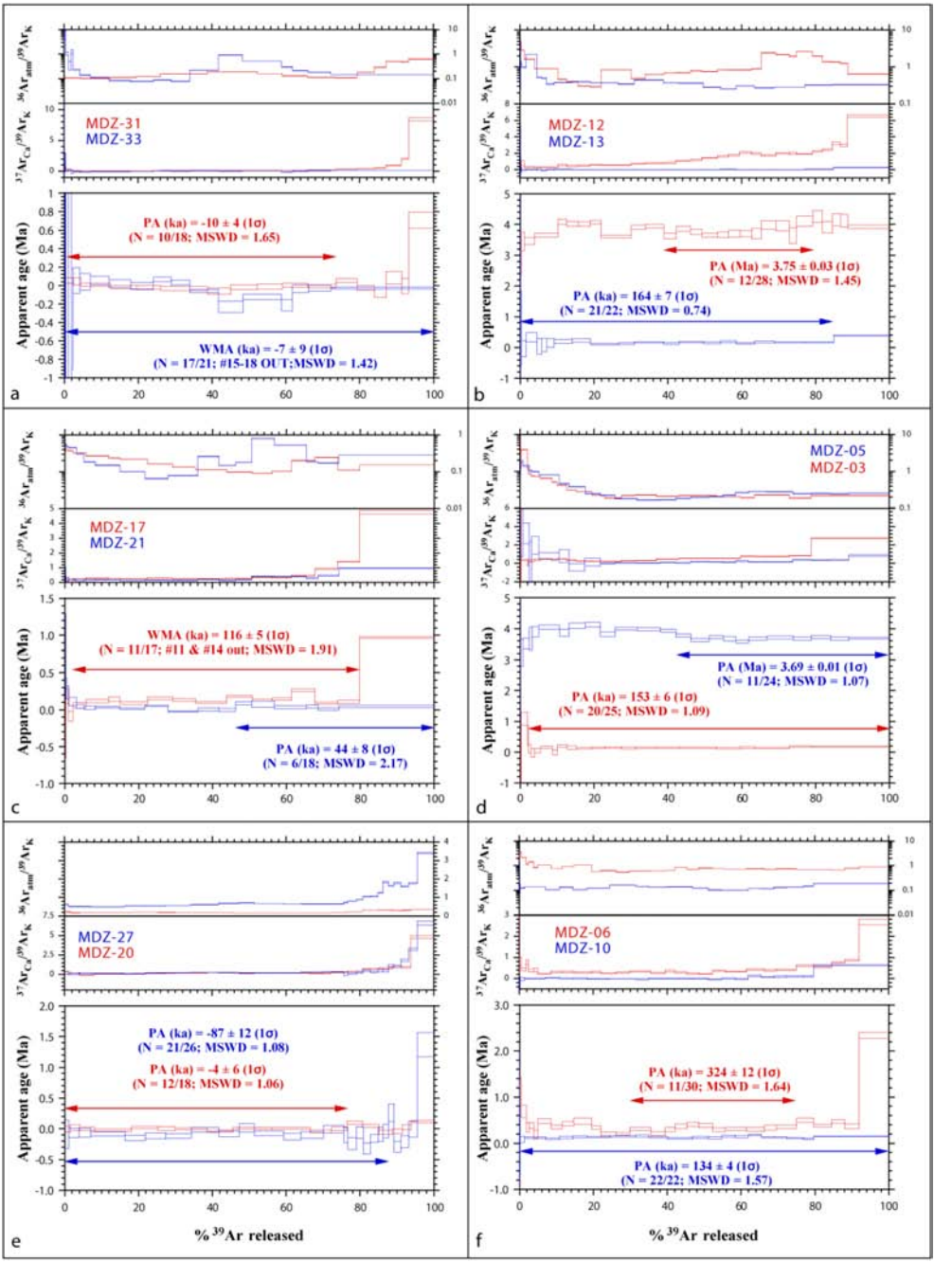
MDZ-31
MDZ-33
PA (ka) = -10 ± 4 (1σ)
(N = 10/18; MSWD = 1.65)
WMA (ka) = -7 ± 9 (1σ)
(N = 17/21; #15-18 OUT;MSWD = 1.42)
Apparent age (Ma)
a
MDZ-12
MDZ-13
PA (Ma) = 3.75 ± 0.03 (1σ)
(N = 12/28; MSWD = 1.45)
PA (ka) = 164 ± 7 (1σ)
(N = 21/22; MSWD = 0.74)
Apparent age (Ma)
b
MDZ-17
MDZ-21
WMA (ka) = 116 ± 5 (1σ)
(N = 11/17; #11 & #14 out; MSWD = 1.91)
PA (ka) = 44 ± 8 (1σ)
(N = 6/18; MSWD = 2.17)
Apparent age (Ma)
c
MDZ-05
MDZ-03
PA (Ma) = 3.69 ± 0.01 (1σ)
(N = 11/24; MSWD = 1.07)
PA (ka) = 153 ± 6 (1σ)
(N = 20/25; MSWD = 1.09)
Apparent age (Ma)
d
MDZ-27
MDZ-20
PA (ka) = -87 ± 12 (1σ)
(N = 21/26; MSWD = 1.08)
PA (ka) = -4 ± 6 (1σ)
(N = 12/18; MSWD = 1.06)
Apparent age (Ma)
e
% 39Ar released
MDZ-06
MDZ-10
PA (ka) = 324 ± 12 (1σ)
(N = 11/30; MSWD = 1.64)
PA (ka) = 134 ± 4 (1σ)
(N = 22/22; MSWD = 1.57)
Apparent age (Ma)
f
% 39Ar released

Figure 10

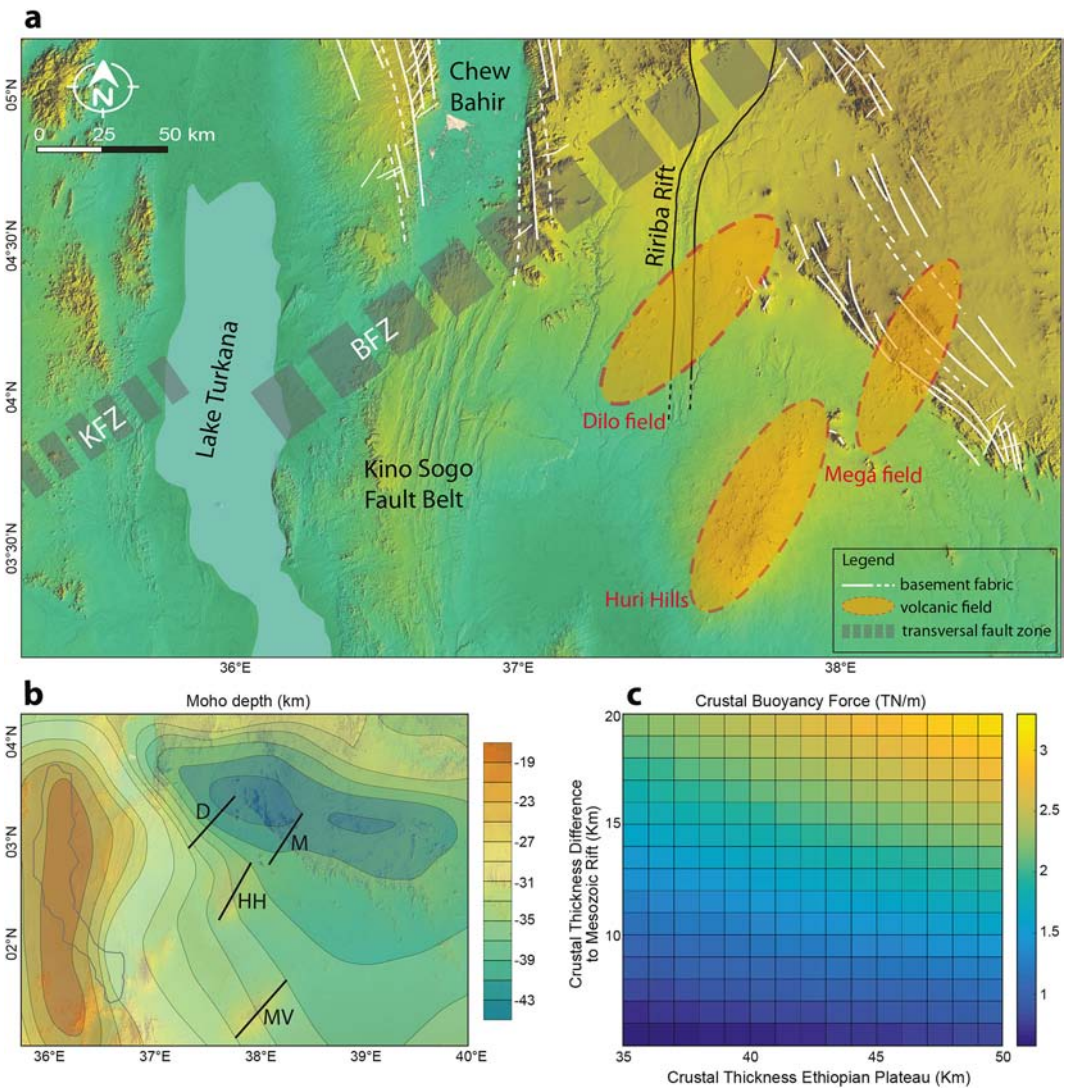
a
Chew Bahir
Ririba Rift
Lake Turkana
BFZ
KFZ
Kino Sogo Fault Belt
Dilo field
Mega field
Huri Hills
Legend
basement fabric
volcanic field
transversal fault zone
0 25 50 km
05°N
04°30'N
04°N
03°30'N
36°E
37°E
38°E
b
Moho depth (km)
D
M
HH
MV
-19
-23
-27
-31
-35
-39
-43
04°N
03°N
02°N
36°E
37°E
38°E
39°E
40°E
c
Crustal Buoyancy Force (TN/m)
Crustal Thickness Difference to Mesozoic Rift (Km)
Crustal Thickness Ethiopian Plateau (Km)
20
15
10
35
40
45
50
3
2.5
2
1.5
1

Figure 11